BOREAS An international journal of Quaternary research

Millennial-scale oscillations and an environmental regime shift around the Middle to Late Holocene transition in the North Atlantic region based on a multiproxy record from Isfjorden, West Spitsbergen

CAMILLE BRICE, ANNE DE VERNAL, PIERRE FRANCUS, MATTHIAS FORWICK AND SEUNG-IL NAM

BOREAS

Brice, C., de Vernal, A., Francus, P., Forwick, M. & Nam, S. I.: Millennial-scale oscillations and an environmental regime shift around the Middle to Late Holocene transition in the North Atlantic region based on a multiproxy record from Isfjorden, West Spitsbergen. *Boreas*. https://doi.org/10.1111/bor.12602. ISSN 0300-9483.

Palynological and sedimentological analyses were performed on the sediment core HH16-1205-GC retrieved from the central Isfjorden, West Spitsbergen. The sequence, which spans the last 7000 years, revealed an overall cooling trend with an important climate shift between 4.4 and 3.8 cal. ka BP, in addition to millennial-scale oscillations. Sea-surface reconstruction from dinocyst assemblages indicates a decrease in summer sea-surface temperature, from 2.5 to 1.5 °C, and primary productivity, from 750 to 650 gC m^{-2} a^{-1} over the last 7000 years. From around 6.8 to 5.8 cal. ka BP, the sedimentological and palynological data suggest a predominant sediment supply from the inner part of the fjord, ice rafting, dense sea ice cover, strongly stratified water masses and high primary productivity. The interval from 4.4 to 3.8 cal. ka BP is marked by a layer of coarser material and a significant decrease in the grain-size mode. Our geochemical data show large-amplitude fluctuations after 2.0 cal. ka BP, while an increase in the dinocysts *Impagidinium pallidum* and *Spiniferites elongatus* from 2.0 to 1.2 cal. ka BP suggests enhanced Atlantic Water inflow. The dinocyst-based reconstructions also reveal large-amplitude millennial fluctuations in sea ice cover, summer sea-surface temperature and salinity. Wavelet analysis and cross-wavelet analysis on K/Ti ratio coupled with sea-ice estimates confirm a strong signal with a periodicity of 1200–1500 years.

Camille Brice (camille.brice@hotmail.com), Université du Québec à Montréal and GEOTOP, Montréal, QC H3C 3P8, Canada (present address: Institut des sciences de la mer, Université du Québec à Rimouski and GEOTOP, 310 Allée des Ursulines, Rimouski, QC G5L 3A1, Canada); Anne de Vernal, Université du Québec à Montréal and GEOTOP, Montréal, QC, H3C 3P8, Canada; Pierre Francus, Centre Eau Terre et Environnement and GEOTOP, Institut National de la Recherche Scientifique, Québec, QC G1K 9A9, Canada; Matthias Forwick, Department of Geosciences, UiT The Arctic University of Norway in Tromsø, Postboks 6050 Langnes, Tromsø N-9037, Norway; Seung-Il Nam, Division of Glacial Environmental Research, Korea Polar Research Institute, Incheon 21990, Korea; *received 18th March 2022, accepted 10th August 2022.*

Along with a decreasing insolation, the Holocene climate in the Northern Hemisphere recorded a gradual cooling in many locations (Berger & Loutre 1991), often following a non-linear trend, sometimes marked by decadal to millennial oscillations (Bond *et al.* 1997; Mayewski *et al.* 2004; Wanner *et al.* 2008). In the northern North Atlantic, these variations suggest quasiperiodic coolings (Bond *et al.* 1997) and were hypothesized to be caused by fluctuations in solar irradiation (Bond *et al.* 2001). Among the cooling pulses, the 4.2 ka event was a major climate anomaly in many parts of the world (Weiss 2017). However, the cause of quasiperiodic cooling pulses ('Bond events'), including the 4.2 ka event, remains controversial. The reviews of palaeoceanographic studies conducted by Wanner *et al.* (2008), Bradley & Bakke (2019), and Geirsdóttir *et al.* (2019) led to the conclusion that the climate in the North Atlantic region has a complex behaviour and that there is no convincing evidence of synchronous cycles and events, including at 4.2 ka BP. Climate oscillations and anomalies are nonetheless recorded, and numerous datasets suggest millennial-scale signals in the North Atlantic region (e.g. Bond *et al.* 1997, 2001; Bianchi & McCave 1999; Klitgaard-Kristensen *et al.* 2001; Schulz & Paul 2002; Sarnthein *et al.* 2003; Mayewski *et al.* 2004; Giraudeau *et al.* 2010; Werner *et al.* 2013). However, the synchroneity, the nature and the causes of the variability remain a matter of debate (e.g. Debret *et al.* 2007; Wanner *et al.* 2008; Wanner & Bütikofer 2008; Goslin *et al.* 2018). The millennial oscillations might have an external triggering forcing related to solar forcing (e.g. Bond *et al.* 2001) and/or internal mechanisms generating self-oscillations the thermohaline circulation (e.g. McManus *et al.* 1999; Broecker 2000; Giraudeau *et al.* 2010). They could also be related to volcanic eruptions (Wanner & Bütikofer 2008; Wanner *et al.* 2011).

The North Atlantic is a key region to study the millennial oscillation as the ocean circulation plays a crucial role in regional climates. The warm and saline Atlantic Water (AW), which is transported northward through the Fram Strait and across the Barents Sea shelf by the Norwegian Altantic Current and the West Spitsbegren Current (WSC), is the main heat source for the Arctic Ocean (Aagaard *et al.* 1985). The AW partly controls the sea-ice extent, which in turn, is a major component of the Northern Hemisphere climate owing to the positive sea-ice albedo feedback (e.g. Serreze & Barry 2011). Seasonal sea-ice formation and melt modify the salinity, affecting density gradients, deep-water

DOI 10.1111/bor.12602

formation and thus the Atlantic Meridional Overturning Circulation (AMOC; e.g. Rudels *et al.* 1996; Dieckmann & Hellmer 2010).

In the northern North Atlantic, the Svalbard archipelago is located between the Fram Strait and the Barents Sea (76–80°N) at the transition between the Atlantic and Arctic oceans (Fig. 1). It is therefore an ideal area for conducting a study on past climate and palaeoceanographic variations to better understand the role of the AW inflow in climate–ice–ocean interactions at high latitudes. The climate of the archipelago depends upon the AW, which flows along its western margin (Nilsen *et al.* 2008). Changes in the strength and thermal properties of the AW directly affect the regional climate, sea-ice distribution and glacier dynamics (Hald *et al.* 2004). The study was carried out in a fjord which contains marine and terrestrial proxies, allowing the reconstruction of both the ocean and land conditions. The fjord waters of western Svalbard are characterized by large temperature and salinity gradients, mainly determined by the inflow of warm and saline AW and cold waters from terrestrial glacier runoff and the melting of tidewater glaciers in addition to Arctic coastal waters. Finally, fjords are characterized by rapid sediment accumulation allowing high temporal resolution records (e.g. Svendsen *et al.* 1992; Hald *et al.* 2004; Forwick & Vorren 2007, 2009; Baeten *et al.* 2010; Forwick *et al.* 2010; Rasmussen *et al.* 2012).

This multiproxy study aims at reconstructing past variations of climate conditions and variability in central Isfjorden, West Spitsbergen. The high sedimentation rate allows high temporal resolution analysis, suitable for identifying oscillations and regime shifts. The data from the analysed sediment core HH16-1205-GC document the surface-water conditions based on dinocyst assemblages, which we use to reconstruct surface ocean parameters (de Vernal *et al.* 2020). We also present the physical and geochemical properties of the sediment, which provide information on bottom-water conditions and terrestrial input. The results bring new insights into the origin of climate and ocean variability over time.

Study area

Physiographic setting

The Svalbard archipelago is located at the gateway to the Arctic, between 74 and 81°N and 10 and 35°E (Fig. 1A). The archipelago is surrounded by the Arctic Ocean to the north, the Fram Strait to the west, the Barents Sea to the east and the Nordic seas to the south. About 57% of Svalbard's surface area is currently covered by glaciers (Hagen *et al.* 1993, 2003; Nuth *et al.* 2013; Pfeffer *et al.* 2014), with many of them terminating in the sea, including in fjords (e.g. Martín-Moreno *et al.* 2017). Spitsbergen is the largest island of Svalbard; it represents more than half of the entire archipelago area. The western coast is characterized by fjords where sea ice typically forms in fall–winter and breaks up in summer (Howe *et al.* 2010). However, the timing of sea-ice formation varies from one year to another (Cottier *et al.* 2007).

The Isfjorden is the largest fjord system on Svalbard and it has the second biggest drainage basin of Spitsbergen (Hagen *et al.* 1993). It is located in the middle of the western coast of the island (78–79°N; 13–17°E; Fig. 1B). The system is about 100 km long and consists of the trunk fjord, Isfjorden, and 13 tributary fjords and bays. Nine tidewater glaciers terminate into the fjord system. The mouth of Isfjorden is about 10 km wide and a sill is absent (Nilsen *et al.* 2008). As a consequence, it is directly connected to the shelf and slope area offshore west Spitsbergen, allowing AW to enter the fjord through the Isfjorden Trough that extends from the fjord mouth to the shelf break.

The geology of the Isfjorden system is dominated by Devonian to Paleogene sedimentary rocks (Fig. 1B; Dallmann 2002). Sandstone, siltstone and shale are observed in the central part of the fjord. The inner part of Isfjorden consists of limestone, chert, silicified limestone and sandstone. Metamorphic rocks of Neoproterozoic phyllites and schists occupy the mouth of the fjord.

Oceanography

Two main water masses influence Svalbard, the AW and the Arctic Water (Nilsen *et al.* 2008). The east coast of Svalbard is dominated by the East Spitsbergen Current, carrying Arctic Water (Fig. 1B). It derives from the Arctic Ocean and flows southward along the coasts of Nordaustlandet and Spitsbergen, turns around the southern tip of Spitsbergen and flows northward as the Spitsbergen Coastal Current (SCC). The AW ($T > 3$ °C, $S > 34.9$ psu) is carried by the WSC, which flows northward along the continental slope of the West Spitsbergen margin, separated from the SCC by the Arctic front (Fig. 1B). The WSC is a northern extension of the North Atlantic Drift. At the latitude of Spitsbergen (~79°N), the AW has lost a considerable amount of heat, increasing the density of the water mass that sinks below the surface (Nilsen *et al.* 2008).

The hydrography in Isfjorden is composed of water masses of external and local origin (Fig. 2). Two external water masses are advected in the system: the AW from the WSC and the Arctic-type water, which consists of Arctic Water freshened by fjord outflows carried northward along the Spitsbergen by the SCC. The AW entering the fjord mixes with the Arctic-type water, resulting in lower temperature and salinity and formation of the so-called transformed Atlantic Water ($T > 1$ °C, $S > 34.7$ psu; Svendsen *et al.* 2002; Cottier *et al.* 2005; Nilsen *et al.* 2008). The intensity of the AW inflow varies annually, increasing in summer and leading to more

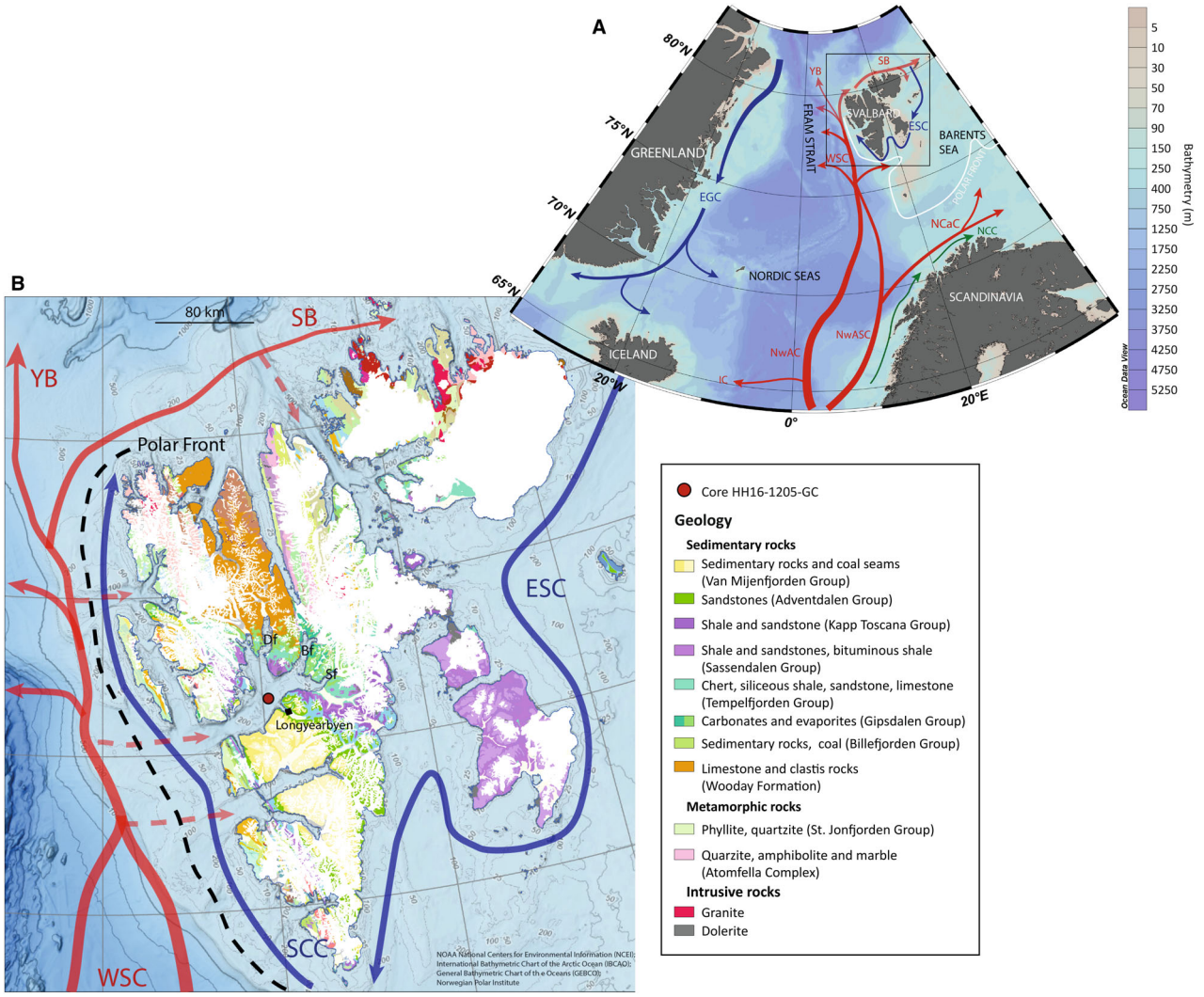

Fig. 1. Maps of the study area. A. Map of the North Atlantic. Red arrows represent the North Atlantic drift with Irminger Current (IC), Norwegian Atlantic Current, Norwegian Atlantic Slope Current (NwASC), North Cape Current (NCaC), West Spitsbergen Current (WSC), Svalbard Branch (SB) and Yermack Branch (YB). The blue arrows represent the Arctic Water flowing via the East Spitsbergen Current (ESC) and the East Greenland Current (EGC). Green arrows are the Norwegian Coastal Current (NCC). The white line indicates the mean position of the Polar Front (Loeng 1991). B. Geological map of Svalbard (data from Norwegian Polar Institute and International Bathymetric Chart of the Arctic Ocean) with the location of the core and the Spitsbergen Coastal Current (SCC). The dashed line represents the general position of the polar front. Df = Dicksonfjorden; Bf = Billefjorden; Sf = Sassenfjorden.

saline and warmer water (e.g. Svendsen *et al.* 2002; Cottier *et al.* 2007; Forwick *et al.* 2010; Jernas *et al.* 2018).

Surface waters ($T > 1$ °C) are mostly local, deriving from glacial melt and river runoff during spring and summer. They occupy the surface layer that decreases in thickness towards the mouth of the fjord (Fig. 2). Autumn and winter cooling of surface waters form local waters ($T < 1$ °C) without significant change in salinity. The Winter-Cooled Waters (WCW; $T < -0.5$ °C, $S > 34.4$ psu) are formed from brine formation and/or intense cooling of the AW. When the WCW becomes denser than the transformed Atlantic Water, it sinks to the bottom of the fjord. Strong formation of WCW can lead to an enhanced inflow of AW in the following summer (Nilsen *et al.* 2008; Rasmussen *et al.* 2012).

Sea ice cover in the Isfjorden system is seasonal. Fast ice starts to form in late November in the tributary fjords and all ice melts at the beginning of the summer (Nilsen *et al.* 2008). Generally, the outer part of the fjord is ice-free throughout the year (Svendsen *et al.* 2002; Nilsen *et al.* 2008; Forwick & Vorren 2009; Rasmussen *et al.* 2012).

Methodology

The 465-cm-long gravity core HH16-1205-GC (78°20.813′N, 015°17.11′E) was retrieved from 259 m water depth in central Isfjorden during the first Korea–

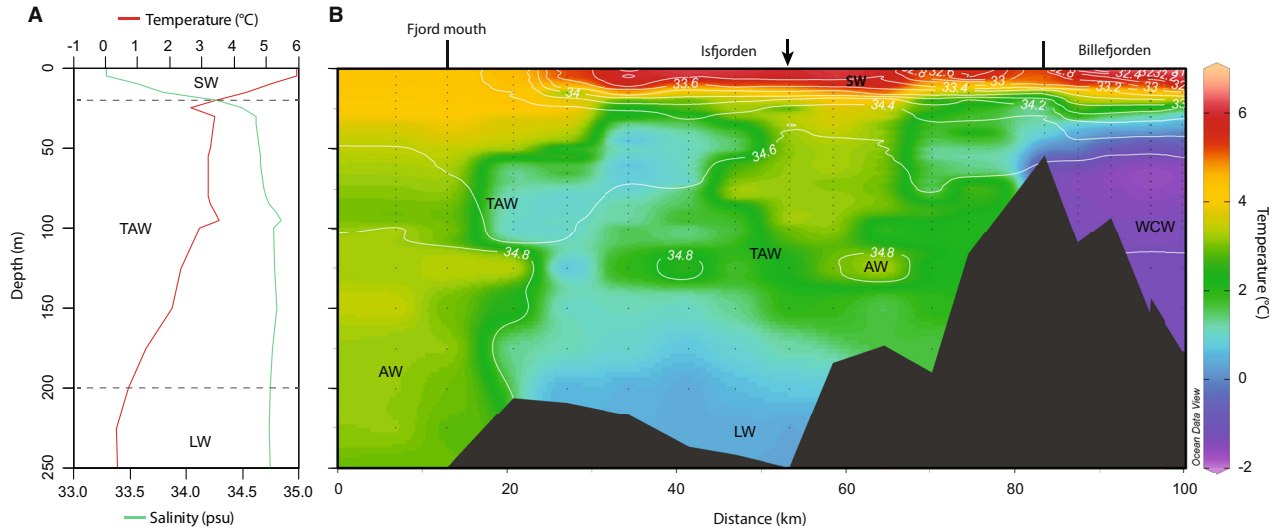

Fig. 2. Conductivity, temperature, depth (CTD) profiles of Isfjorden. AW = Atlantic Water; TAW = Transformed Atlantic Water; WCW = Winter Cooled Water; LW = Local Water; SW = Surface Water. A. CTD profile taken in July 2018 at the station 19272345 (B) (78°18.3′N; 15°25.38′E), close to core HH16-1205-GC site. B. CTD section from Isfjorden mouth to Billefjorden along the southern side of the fjord in July 2018. Salinity is given by white contour lines. The black arrow points to the location of station 19272345 (B). Data were retrieved from World Ocean Database 2018 (Boyer *et al.* 2018).

Norway joint cruise with RV 'Helmer Hanssen' of UiT The Arctic University of Norway in July 2016.

Sedimentology

Prior to core splitting, the physical properties (wet-bulk density, magnetic susceptibility, p-wave velocity and amplitude, fractional porosity) were measured in 1-cm steps using a GEOTEK multisensor core logger. Wet-bulk density was measured using a gamma source of ^{137}Cs and calculated from the gamma density with the calibration made using an aluminium cylinder (Geotek 2000). X-radiographs were acquired from whole-core sections and half-core sections using a GEOTEK XCT system. A lithological description of the sediments included visible variations in grain size, fossil and clast contents, bioturbation, colour and sedimentary structures.

Non-destructive qualitative element-geochemical measurements of the surfaces of half-core sections were carried out with an Avaatech X-ray fluorescence (XRF) core scanner. The data acquisition was made at 1-cm intervals with an exposure time of 10 s at a voltage of 10 kV, a current of 1000 μA and no filter for Al, Si, S, Cl, K, Ca, Ti, Mn and Fe, and with 30 kV and 2000 μA with a Pb thick filter for Rb, Sr and Zr. To minimize the matrix effect, such as variations in intensities owing to an uneven surface or a thin water film (Tjallingii *et al.* 2007; Weltje & Tjallingii 2008), data are interpreted as element log-ratios rather than results from single elements. All of the above-mentioned measurements were carried out at the Department of Geosciences at UiT The Arctic University of Norway.

After the non-destructive measurements, the core was subsampled for 1-cm-thick slices at every 5 cm for granulometric analyses. The samples were freeze-dried, and ~300 mg were treated with 10% H_2O_2 to decompose the organic matter. After rinsing with distilled water, the samples were treated with an ultrasonic vibrator for 15 s to keep particles in suspension and facilitate dispersion. Grain-size analysis was performed at the Korea Institute of Geoscience and Mineral Resources, Daejeon, Korea, using a Mastersizer 2000 laser analyser. It provides the grain-size percentage for several size categories and calculates the percentage of clay, silt and sand, as well as the median grain size of samples. The results were then analysed using GRADISTAT (Blott & Pye 2001) to calculate the arithmetic distribution mode.

Chronology

The chronology of the studied core is based on six AMS ^{14}C dates from mixed benthic foraminifer tests and bivalve shells. Radiocarbon dating was performed on the mini radiocarbon dating system at the Alfred Wegener Institute, Helmholtz Centre for Polar and Marine Research in Bremerhaven, Germany. The AMS ^{14}C dates are reported using the Libby half-life of 5568 years. Calibration was performed using the Marine13 calibration curve (Reimer *et al.* 2013) with an additional correction (ΔR) of 90±35 ^{14}C years for the regional air–sea reservoir (Mangerud & Gulliksen 1975). The Marine20 calibration curve was not used as it is not suitable for polar regions (Heaton *et al.* 2020). The age–depth model was computed using the software Bacon 2.2 (Blaauw & Christen 2011) run under R (R Core

Team 2021). Bacon relies on a Bayesian approach and applies many iterations to create the 'best model' within a confidence interval.

Microfossils analysis

Subsamples used for grain-size analyses were also used for palynological analyses. Each sample was processed according to de Vernal *et al.* (2010). One to two grams were collected and sieved at 106 and 10 μm. The dried fraction >106 μm, mainly composed of detrital material, was weighed and used for hand-picking of biogenic carbonate. The 10–106 μm fraction was used for palynological preparations, which consisted of chemical treatment with HCl (10%) and HF (49%) to dissolve carbonate and silica particles, respectively. The residues were mounted on microscope slides with glycerin gelatin. *Lycopodium clavatum* spore tablets (batch no. 938934 with n = 10 679±426 spores/tablet and no. 3862 with n = 9666±671 spores/tablet) were added to the samples to estimate palynomorph concentration (e.g. Mertens *et al.* 2009).

The palynological analyses consisted of identification and counts of all palynomorphs on the slides, including pollen grains, spores, dinocysts, *Halodinium* and foraminifer organic linings. The observations were made with an optical microscope in transmitted light at magnifications of ×400–1000. Reworked pre-Quaternary dinocysts, pollen grains, spores and acritarchs were also counted. A minimum of 300 dinocysts was counted and identified in each sample. The taxonomic nomenclature of dinocysts was based on Rochon *et al.* (1999) and Radi *et al.* (2013), updated by Van Nieuwenhove *et al.* (2020). The relative abundances of dinocyst taxa were expressed as percentages compared with counted dinocysts. Uncertainties on relative abundance are ±4% with a probability of 0.95 and ±2.5% with a probability of 0.75 after statistical analysis conducted with the 'statcounts' Excel add-in developed by Heslop *et al.* (2010). Pollen grains and spores were used to quantify terrestrial inputs, and reworked palynomorphs as indicators of erosion of old sedimentary material, subsequent transport and re-sedimentation. The concentration of palynomorphs is expressed as the number of specimens per gram of sediment, with an approximate error of ±10% for a confidence interval of 0.95 (de Vernal *et al.* 1987; Mertens *et al.* 2009). Fluxes were estimated using sedimentation rates based on ^{14}C dating and the density calculated from multisensor core logger measurements.

Reconstruction of sea-surface conditions

Sea-surface temperature (SST; °C) in winter and summer, sea-surface salinity (SSS; psu) in winter and summer, sea ice cover (months per year >50%) and primary productivity (gC m^{-2} a^{-1}) were reconstructed from dinocyst assemblages based on the application of the modern analogue technique (MAT; Guiot & de Vernal 2007) using the new database of the Northern Hemisphere, which includes 1968 reference sites and 71 taxa (de Vernal *et al.* 2020). The MAT has been applied with the package 'rioja' running under R (Juggins 2017). The reconstructions were made from the five best modern analogues as identified from the distance calculation (inversely proportional to the similarity) after log-transformation of percentage data. In the case of the n = 1968 database, the threshold distance for good analogues is 1.2. The sea-surface conditions at the five selected modern analogue sites define the maximum, minimum and most probable values associated with the assemblage, which correspond to the average weighted inversely to the distance. The distance can be used as an indicator of the quality of the reconstruction: the lower the distance, the higher the similarity of the modern analogue, and therefore, the better the reliability of the estimate is. Tests to evaluate the accuracy of the approach with the leaving-one-out approach indicate good correlations between observations and reconstructions, with $r^2 > 0.961$ for SST, >0.736 for SSS, 0.843 for sea ice and 0.874 for productivity. The errors of prediction are ±1.16 and ±1.75 °C for winter and summer SST, ±1.0 and ±2.0 for winter and summer SSS, ±1.5 months/year for the sea ice cover and ±95 gC m^{-2} a^{-1} for productivity. The MAT as any transfer function approach has weaknesses that are discussed on statistical bases in many articles (e.g. Guiot & de Vernal 2007, 2011; Telford & Birks 2009; Hohmann *et al.* 2020; Chevalier *et al.* 2020). In view of the non-linearity of the environment vs. assemblage relationship, the analogue approach is more appropriate than calibration techniques. The reconstructions made with dinocysts assemblages are based on a large data sets, including several taxa and diverse environmental conditions. They furthermore rely on counts being statistically representative and based on close analogous assemblages. Hence, we are confident that reconstructions are reliable, within the uncertainties provided by the set of analogues selected and their distances, in addition to overall error of prediction.

Time-series analysis and quantitative treatment

Multivariate analyses were performed on the data and the methodology together with the results can be found in Data S1.

For estimating the frequency spectrum of our data, we used the Lomb–Scargle periodogram (Lomb 1976; Scargle 1982), a method for detecting periodic signals on uneven sampled time series. The application for the algorithm was done with the R package 'Lomb' (Ruf 1999). p-Values for the highest peak in the periodogram are computed from the exponential distribution.

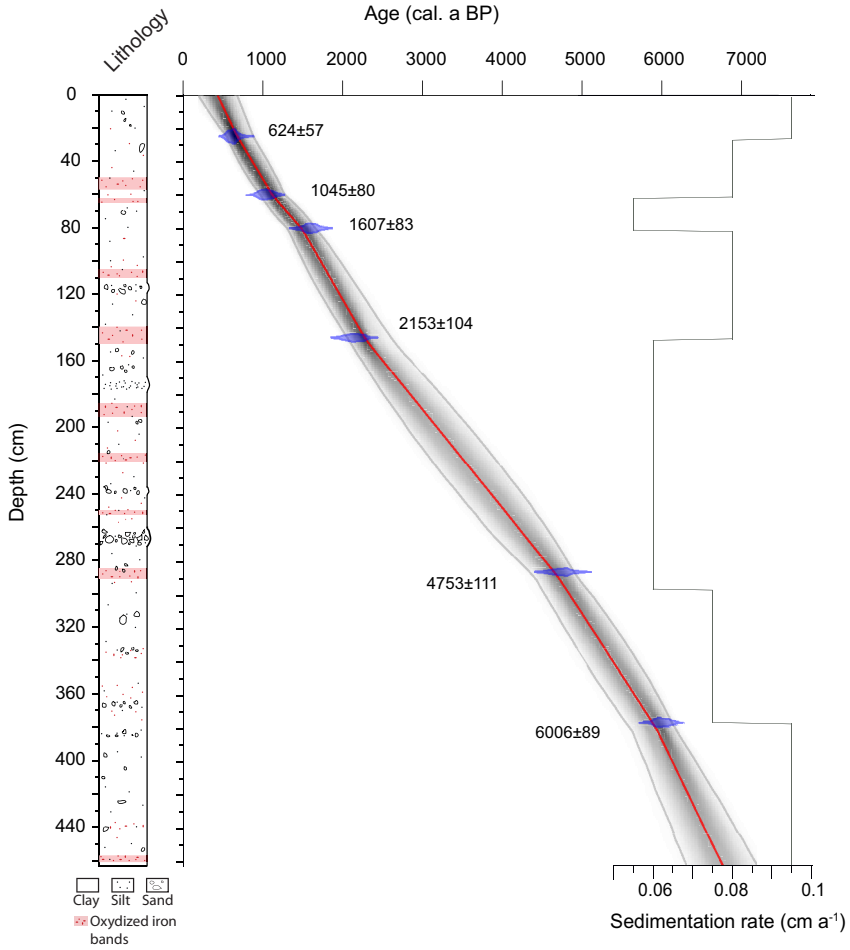

Fig. 3. Lithological description, age–depth profile and sedimentation rate of core HH16-1205-GC. Age vs. depth relationship was modelled with the R package BACON based on ^{14}C chronological dates.

Wavelet analysis was performed with the R package 'WaveletComp' (Roesch & Schmidbauer 2018). Since wavelet analysis requires evenly spaced time series, our data were first interpolated using a fast Fourier transformation. No detrending was made on the data for the analysis. Wavelet analysis was performed with a time resolution of one time unit, a frequency resolution of 1/100, and the 'white noise' method with 10 simulations. The same arguments were used for cross-wavelet analysis between sedimentological and palynological data, except that the frequency resolution was 1/50 and five simulations were made.

Results

Chronology

The chronology of core HH16-1205-GC reveals sedimentation rates between 0.055 and 0.095 cm a^{-1}, with a mean rate of ~0.7 cm a^{-1} throughout the study sequence (Fig. 3, Table 1). Extrapolation indicates that the sediments at the bottom of the core were deposited at around 6770 cal. ka BP. The time resolution of analyses is ~10 years for non-destructive analyses and ~50 years for palynology and grain size.

Physical properties

The sediments are mainly composed of silt and clay. At the bottom of the core, slightly coarser material than at the top was recovered, with a median size between 6 and 7.5 µm, decreasing to ~5.5 µm towards the top (Fig. 4). The silt content gradually decreases from 65 to ~57%, while the clay content increases from ~33 to 40% (Fig. S1). Sand is nearly absent, apart from two layers containing a significant amount (9–12%) observed at 6.2 and 4.4 cal. ka BP. The layer of coarser material at 4.4 cal. ka BP, which is mostly composed of unsorted very fine sand (noted during lithological description; Fig. 3), marks a change in median grain size. Higher and more fluctuating values are recorded beneath this layer, whereas lower and more stable values are documented above.

Table 1. Radiocarbon dates of core HH16-1205-GC and corresponding calibrated ages. The calibration was made with a ΔR of 90±35 ^{14}C years on BACON with the Marine13 calibration curve.

AWI no.	Sample ID (depth in cm)	^{14}C dates (a BP)	Calibrated years BP ranges		Mean age (cal. a BP)	Dated material
			1 sigma	2 sigma		
1941.1.1	24–25	1148±62	553–673	508–745	624	Benthic foraminifer, bivalve shell fragments
1942.1.1	59–60	1581±60	959–1125	905–1213	1045	Benthic foraminifer, bivalve shell, gastropod
1943.1.1	79–80	2126±62	1519–1696	1416–1791	1607	Benthic foraminifer, bivalve shell
1944.1.1	144–145	2582±72	2064–2276	1946–2329	2153	Benthic foraminifer, bivalve shell fragments
1945.1.1	284–285	4650±78	4657–4854	4511–4975	4753	Benthic foraminifer, bivalve shell fragments
1946.1.1	374–375	5693±65	5910–6094	5841–6168	6006	Benthic foraminifer, bivalve shell fragments

Two intervals, A and B, can be distinguished based on the grain-size distribution mode (Fig. 4). At the bottom of the core, the modes vary between 8.2 and 9.4 μm, with peaks at 11.8 μm. At 4 cal. ka BP, there is a transition towards lower values, mostly around 8.2 μm. The distribution mode is 7 μm from 2.2 to 1.2 cal. ka BP. In the uppermost interval, from 1.2 to 0.4 cal. ka BP, values fluctuate between 8.2 and 7 μm.

Bulk density and magnetic susceptibility do not show large variations throughout the core. Yet a slight decrease is observed with density decreasing from 1.55 to 1.45 g cm^{-3} and magnetic susceptibility from 20 to 13 × 10^{-5} SI upward. Magnetic susceptibly records variations in accordance with those of median grain size, with higher values until 4.4 cal. ka BP and lower values afterward. A significant decrease in bulk density and magnetic susceptibility is recorded from 1.25 to 1.1 cal. ka BP with a minimum of 1.35 g cm^{-3} and 12 × 10^{-5} SI, respectively.

Geochemistry

Measurements of organic carbon reveal values that suggest high productivity and/or low organic matter oxidation (Fig. 4). The C_{org}:N ratios vary around 10 until 3.2 cal. ka BP and then gradually increase to 14–15. Such C_{org}:N values indicate a mixed origin of the organic carbon with a slight shift towards terrestrial values in the upper half of the core (Meyers 1997; Knies & Martinez 2009). The $CaCO_3$ content fluctuates between 0% and ~8%. The highest values are recorded in the lower part of the core, the lowest values at 3.6–3.4 cal. ka BP and moderately high values in the upper part of the core. Carbonates are mostly of detrital origin, as indicated by the rarity or absence of the foraminifera and other biogenic carbonate remains in studied samples.

The XRF core scanner measurements of eight elements kept for the study (Al, Si, K, Ca, Ti, Mn, Fe, and Sr) were plotted as element log ratios (Fig. 5).

A Loess regression was applied to ratios with a degree of smoothing of span = 0.15 to mitigate the noise in the results (Cleveland & Devlin 1988). The results were also plotted against their sum (Fig. S2) to better illustrate single element variations. The geochemical composition of the sediment at the bottom of the core (6.8–5.8 cal. ka BP) shows high Sr and Ca fluctuating values (Fig. S2) that decrease upward. Covariation of both elements usually suggests that Ca mainly originates from biogenic $CaCO_3$ (e.g. Carlson *et al.* 2008). However, low and relatively stable $CaCO_3$ content is inconsistent with the XRF indicators. The Ca/Ti and Sr/Ca ratios, which are commonly used to characterize whether the calcium is from a terrigenous or biogenic source (Rothwell & Croudace 2015), show large amplitude fluctuations, highlighting a signal of both detrital and biogenic carbonates (Rothwell & Croudace 2015). An explanation for such a mixed signal might be a change in the main source of detrital sediments at our site.

At 4.2 cal. ka BP, a significant change is recorded in Mn (Figs 5, S2). Lower and more stable values of Mn/Fe characterize the lower part of the core, while higher and fluctuating values are recorded between 4.2 and 1.8 cal. ka BP. An increase in the Mn content compared with Fe indicates a change in sediment provenance and/or water oxygen levels as both Mn and Fe are redox-sensitive elements. Because Fe oxidizes more rapidly than Mn, a high Mn/Fe ratio usually indicates a shift towards higher dissolved oxygen levels in bottom waters (Naeher *et al.* 2013; Rothwell & Croudace 2015). However, using the Mn/Fe ratio as a proxy of oxygenation is not straightforward as several factors, such as terrestrial inputs and bioturbation, may intervene.

Large-amplitude variations are observed in all ratios and element relative abundances of the sediment encompassing the past 2000 years. The variations are particularly well expressed by the log-ratios of Mn/Fe, K/Al and Fe/Ti (Fig. 5). The most significant variation is recorded at ~1.3 cal. ka BP, when all of the ratios mentioned above

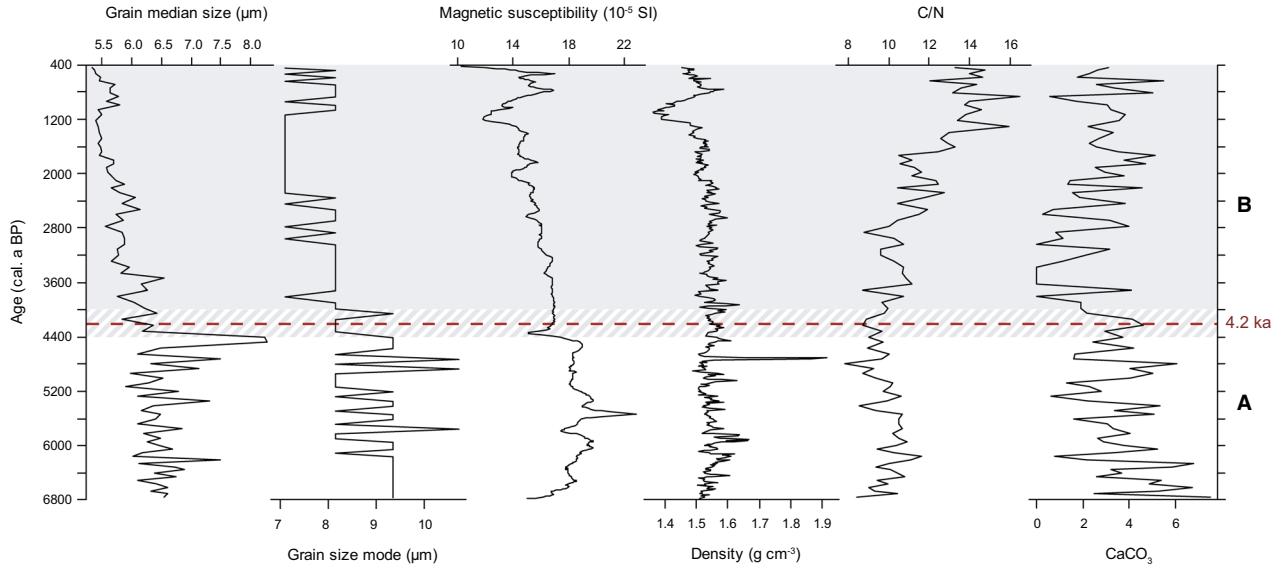

Fig. 4. Grain size distribution (median and mode), magnetic susceptibility, density, ratio of carbon vs. nitrogen (C/N) and percentage of carbonates ($CaCO_3$) in bulk sediment of core HH16-1205-GC. Zones defined as Middle (A) and Late Holocene (B) are indicated to the right.

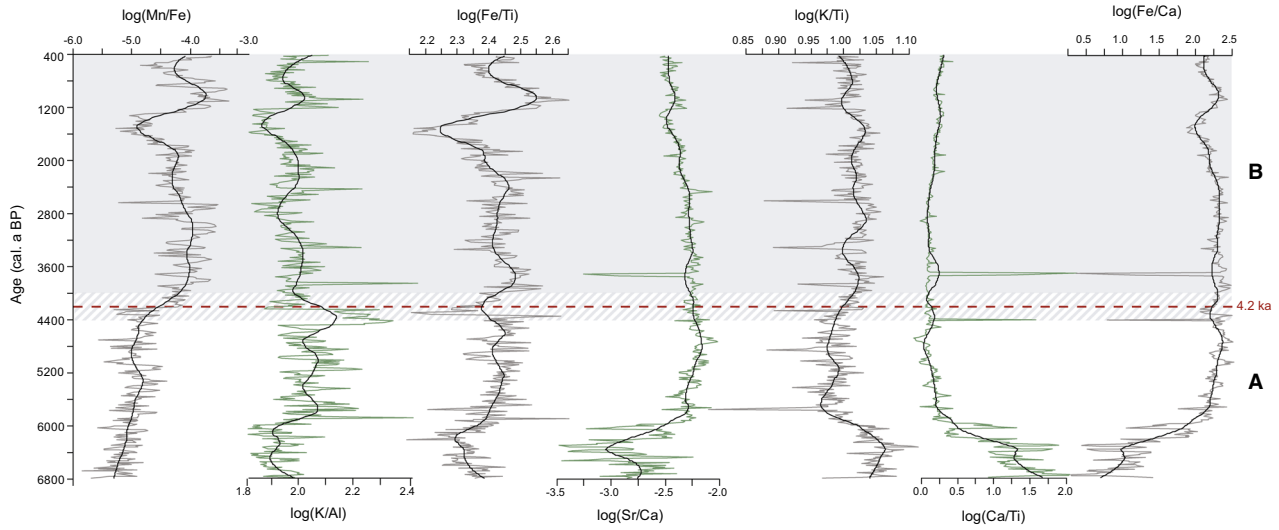

Fig. 5. Geochemical content in sediment of core HH16-1205-GC expressed as element log-ratios. Grey and green lines represent the log-ratio values and black lines represent the smoothed values after Loess regressions. Zones defined as Middle (A) and Late Holocene (B) are indicated to the right.

increase sharply. The Fe/Ca ratio also varies but with a lower amplitude.

Palynology

Dinocysts and other palynomorphs. – Palynological counts revealed dinocyst concentrations between 10 000 and 30 000 cysts g^{-1}, leading to calculate fluxes of 1000–5000 specimens cm^{-2} a^{-1}, and up to 10 000 specimens cm^{-2} a^{-1} at 6.65 cal. ka BP (Fig. 6). Such values indicate very high productivity. The highest values are recorded at the bottom of the core, with fluxes gradually decreasing towards the core top. *Halodinium* sp., which belongs to ciliates (Gurdebeke *et al.* 2018) and mostly occurs in coastal estuarine environments, is abundant throughout the core (2000–12 000 specimens g^{-1}), which also evidences high productivity. All palynomorphs record a general decrease in their concentrations upcore.

Islandinium minutum largely dominates the dinocysts assemblage, with relative abundances varying between 40 and 80% (Fig. 6). This species is associated with cold

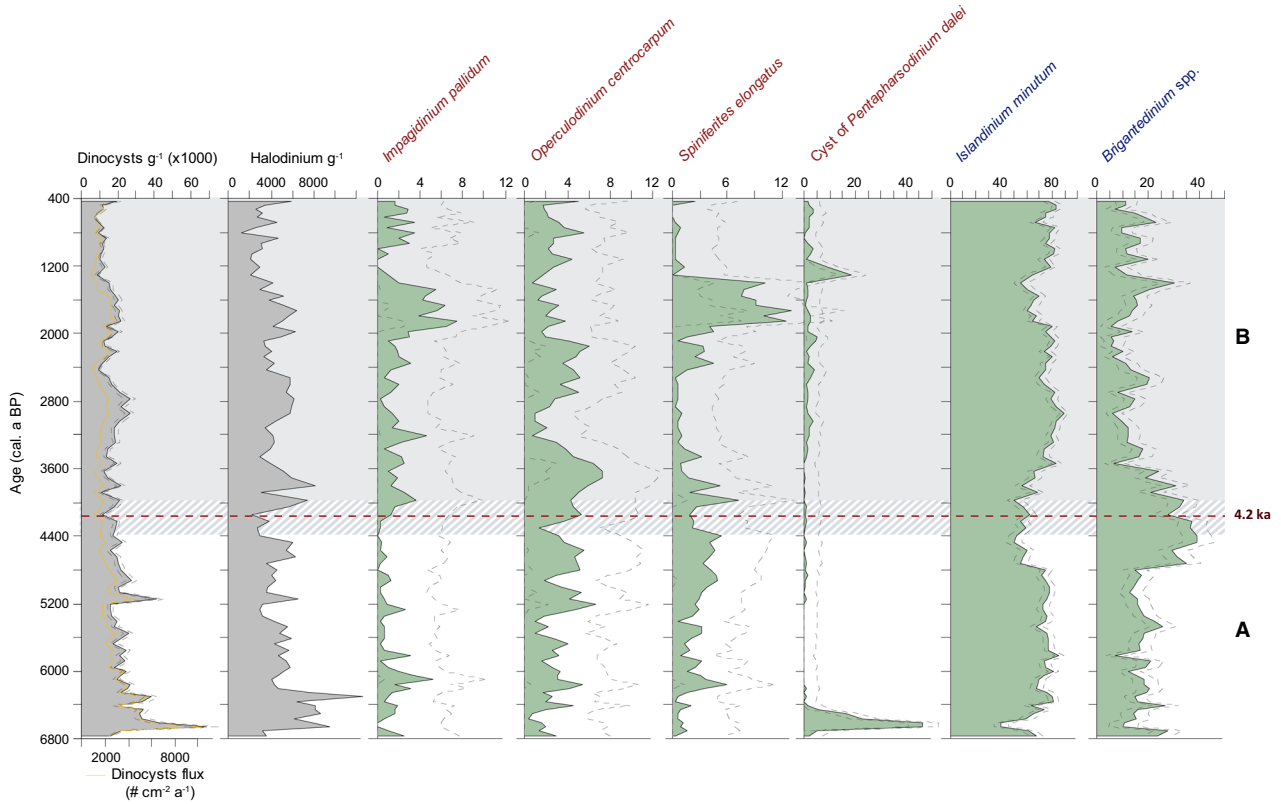

Fig. 6. Concentration of dinocysts and *Halodinium*, and percentages of the main dinocyst taxa in core HH16-1205-GC. Broken lines indicate the upper and lower limits of the 95% confidence interval. Species written in red are phototrophic and those in blue are heterotrophic. Zones defined as Middle (A) and Late Holocene (B) are indicated to the right.

conditions (cf. de Vernal *et al.* 2013, 2020) and is typical of Arctic fjords (Grøsfjeld *et al.* 2009). Other taxa include the cosmopolitan heteroptroph taxon *Brigantedinium* spp. and phototroph taxon *Operculodinium centrocarpum*, the boreal–polar taxa cyst of *Pentapharsodinium dalei* and *Spiniferites elongatus*, and the boreal–subarctic taxon *Impagidinium pallidum* (de Vernal *et al.* 2020). Both *S. elongatus* and *I. pallidum* are characteristic of surface sediments from the Nordic seas under the influence of relatively warm and saline AW (Bonnet *et al.* 2010). The lowest centimetres of the core, which represent less than 100 years, are mainly composed of the heterotrophic taxa *I. minutum* and *Brigantedinium* spp, accounting for ~90% of the assemblage. From 6.7 to 6.5 cal. ka BP, an abundance peak of the cyst of *P. dalei*, which reaches 47%, is recorded. At 6.5 cal. ka BP, the cyst of *P. dalei* drops to 20% while *I. minutum* increases back again. Following this interval, the assemblages are dominated by *I. minutum* (~75%) and *Brigantedinium* spp. (~15%), accompanied by *I. pallidum*, *O. centrocarpum* and *S. elongatus*. Between 4.8 and 3.6 cal. ka BP, an increase in *Brigantedinium* spp (30–40%) at the expense of *I. minutum* (~60%) is recorded, while *I. pallidum* recorded higher percentages starting at 4.2 ka BP. The interval spanning 2.0–1.3 cal. ka BP is characterized by an increase in phototrophic taxa such as *S. elongatus* (9–13%) and *I. pallidum* (4–7%), as well as a slight decrease in *I. minutum* (50%). From 1.3 cal. ka BP to present, the assemblages are similar to those of the interval from 3.6 to 2.0 cal. ka BP.

Quantitative reconstruction of sea-surface conditions. – The application of MAT yielded reconstructions based on five close analogues for every sample. The distance between fossil spectra and modern analogues never exceeded the value of 0.35. The analogues come from different areas, which results in high-amplitude variations of sea-surface parameters. A high number of analogues are from eastern and northern Baffin Bay, with some of them located close to western Greenland fjords. The majority of the other analogues are from the Fram strait or close to an eastern Greenland fjord. Loess regression was applied to the estimated SST, SSS, sea ice and productivity to better visualize the trends, with a degree of smoothing of span = 0.15. Yet the smoothed MAT results (Fig. 7) revealed variations of sea-surface conditions marked by a general trend in addition to cyclical variations.

The base of the core (6.8–6.7 cal. ka BP) starts with a sharp increase in productivity, from 300 to 950, and from

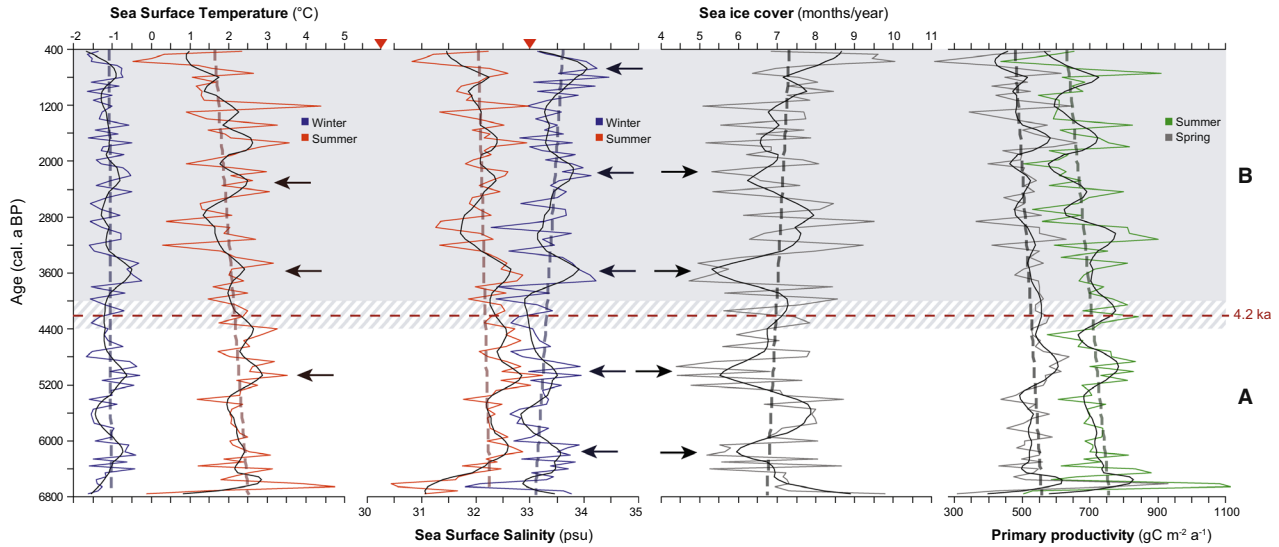

Fig. 7. Sea-surface conditions reconstructed using the modern analogue technique to the dinocyst assemblages of core HH16-1205-GC. Sea-surface temperatures (SST) in summer and winter are represented by red and blue curves, respectively. Summer and winter sea surface salinities (SSS) are shown by the red and blue curves; and sea ice cover, and summer and spring primary productivity are shown by green and grey lines. Black curves correspond to smoothed values after Loess regressions. Red triangles indicated current summer SST and summer SSS. Zones defined as Middle (A) and Late Holocene (B) are indicated to the right.

500 to 1100 gC m^{-2} a^{-1}, in spring and summer, respectively. Summer SST increases from 0 to 4.5 °C, while winter SST remains slightly below the freezing point. The SSS decreases from 31 to 30.5 psu in summer and from 33.5 to 32 psu in winter. The sea ice cover is ~9.5 months/year at the bottom of the core but immediately decreases to 7 months/year after. The productivity and temperature maxima, which coincide with salinity minima recorded between 6.7 and 6.6 cal. ka BP, correspond to maximum percentages of the cyst of *Pentapharsodinium dalei*, a common taxon of sub-Arctic regions occurring in a wide range of salinity conditions (e.g. Matthiessen *et al.* 2005; de Vernal *et al.* 2013, 2020).

A trend towards colder conditions can be distinguished from the MAT results. Throughout the core, from base to top, summer SST decreases by about 1 °C, winter SSS increases by 0.5 psu and sea ice cover gains 0.5 month/year coverage. A reduction in summer and spring productivity by 125 and 100 gC m^{-2} a^{-1}, respectively, is also observed. In addition to the linear trend, cyclic fluctuations are recorded for all variables and more distinctively the sea ice cover, which records large-amplitude variations between 5 and 9 months/year. Maxima in summer SST and winter SSS correspond to sea ice cover minima and *vice versa* (see arrows in Fig. 7). High SSS and SST associated with low sea ice coverage suggest a dominant AW signal.

Spectral analysis

The application of the Lomb–Scargle algorithm highlighted different oscillations within the time series (Fig. 8). Two strong signals were detected with periods around 1260 and 1580 years. In the XRF data, there is a periodicity of 1269 years for K/Al and K/Ti and of 1587 years for Fe/Ti. The dinocysts concentrations record a periodicity of 1582 years and that of sea ice cover a periodicity of 1265 years. A similar periodicity was detected for the relative abundance of *Operculodinium centrocarpum*. It is also discernible from the analyses of all sea-surface parameters, but the signal is unclear.

Wavelet analysis led to distinguish similar periodic signals for several parameters (Fig. 9). A period of ~1300 years characterizes the relative abundance of *O. centrocarpum* from 6.8 to 1.5 cal. ka BP. Sea ice cover exhibits a cyclicity with a periods of ~1300 years between 6.8 and 2.0 cal. ka BP and a period of 150–250 years throughout the sequence. Both winter SST and SSS show a 1300-year cycle (not shown). Three XRF ratios showed a signal, which is, however, unclear. Log(Fe/Ti) exhibits an oscillation with a period of ~1300 years over the last 3.5 ka. Log(K/Ti) has a decreasing periodicity from ~1500 years in the lower part of the core to ~1100 years in the upper part of the sequence. The results for log(K/Al) show a weak periodicity of ~1100 years, but there seems to be a stronger one of ~700 years.

Cross-wavelet analysis between log(K/Ti) and sea ice cover shares a common stable periodic signal of ~1200 years. Both parameters are in opposition until 4.0 cal. ka BP, but after 3.0 cal. ka BP, the signal is weaker and the parameters are in phases. No significant cycle is observed in cross-wavelets between the log(Fe/Ti) and the winter SST until 4.0 cal. ka BP. However, from

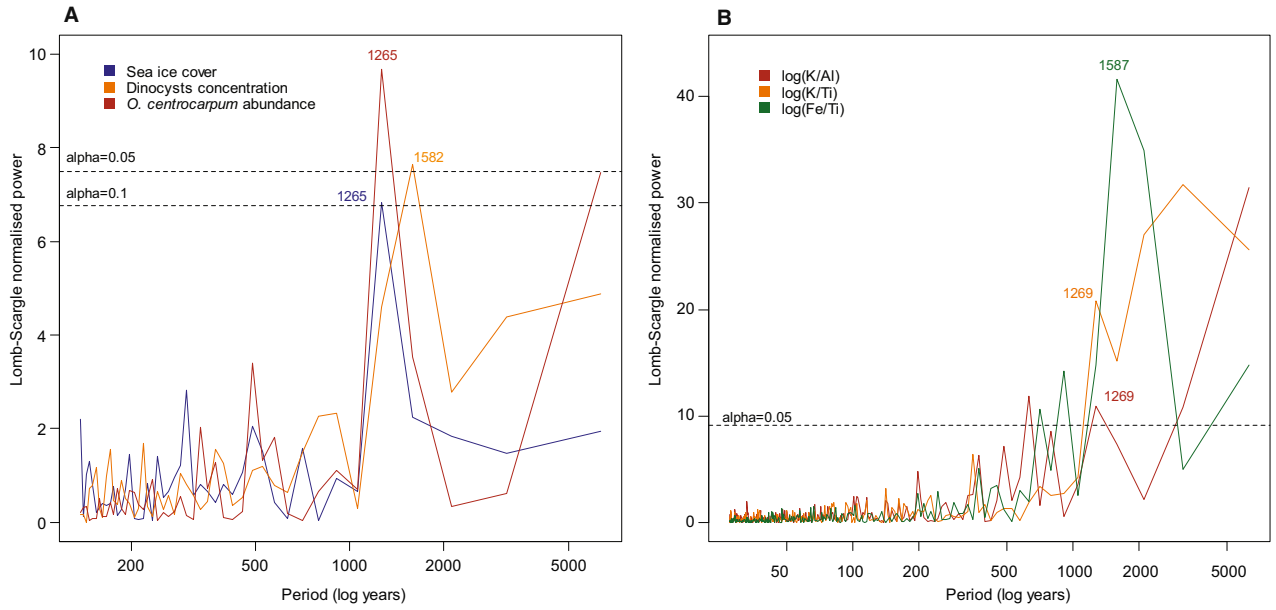

Fig. 8. Periodicity of (A) reconstructed sea ice cover, dinocyst concentration and relative abundance of *Operculodinium centrocarpum* and (B) XRF log-ratios K/Al, K/Ti and Fe/Ti computed from a Lomb–Scargle periodogram. Significance levels (alpha) were established at 5% (A and B) and 10% (A). Peak values are 1265 years for sea ice cover and *Operculodinium centrocarpum* and 1582 years for dinocyst concentrations, 1269 years for K/Al and K/Ti and 1587 years for Fe/Ti.

4.0 cal. ka BP to the present, both the log(Fe/Ti) and the SST seem to be in phase with a ~1200-year cycle.

Discussion

Holocene cooling trend

An overall climate deterioration characterized the last 7 ka in Isfjorden. The MAT reconstructions show an apparent decline in SST and growth of sea ice cover, which may result from the cooling of the Atlantic Water entering the fjord, as suggested by Rasmussen *et al.* (2012). A reduction of primary productivity owing to colder surface waters is also depicted in C_{org}:N values, which shifted from marine to terrestrial input during the Middle to Late Holocene.

On a local scale, the trend of increasing winter SSS was probably caused by lower meltwater discharge and more brine from sea-ice formation, while the summer SSS slightly decreased because of the melting of sea ice. The median grain size indeed decreased, thus suggesting deposition under quieter conditions. A general diminution in current strength related to a reduction of AW inflow, less meltwater discharge and/or denser sea ice cover are factors that may explain the prevalence of a less energetic sedimentary regime.

The Holocene cooling of the AW owing to declining insolation has been documented in many studies from the NE North Atlantic (Koç *et al.* 2002; Sarnthein *et al.* 2003; Andersen *et al.* 2004; Hald *et al.* 2004; Ślubowska *et al.* 2005; Rasmussen *et al.* 2007, 2012; Forwick & Vorren, 2009; Werner *et al.* 2013; Falardeau *et al.* 2018). However, the climate deterioration recorded in these studies and in ours was not linear and occurred through stepwise transitions, with multi-decadal to century-scale coolings (Wanner *et al.* 2011). In the central Isfjorden, a series of events are recorded superimposed on the general cooling around the transition from Middle to Late Holocene. However, given the uncertainties in the age model, which is based on mixed carbonate material with potential age offsets between foraminifers and mollucs (Heier-Nielsen *et al.* 1995), the timing of the events has to be considered cautiously.

Zone A: Middle Holocene (6.8 to 4.2 cal. ka BP)

The time interval identified as 'Zone A' in our dataset corresponds to the Middle Holocene. It is characterized by fluctuations in median grain size that suggest variations in the depositional environment, and C_{org}:N values that indicate mixed terrestrial and marine sources of organic matter. A trend towards more ventilated bottom water is also observed as shown by an increase in the Mn/Fe log-ratio.

Zone A starts with a short but marked event, as observed by the high values in several proxies at the base of the sediment core (Fig. 7). The Ca and Sr signal indicates a mixed detrital and biogenic carbonate source, although it is inconsistent with the $CaCO_3$ data. The highest values of log(K/Ti), an indicator for terrigenous material input as the K main source is weathered sedimentary rocks (Diekmann *et al.* 2008; Rothwell &

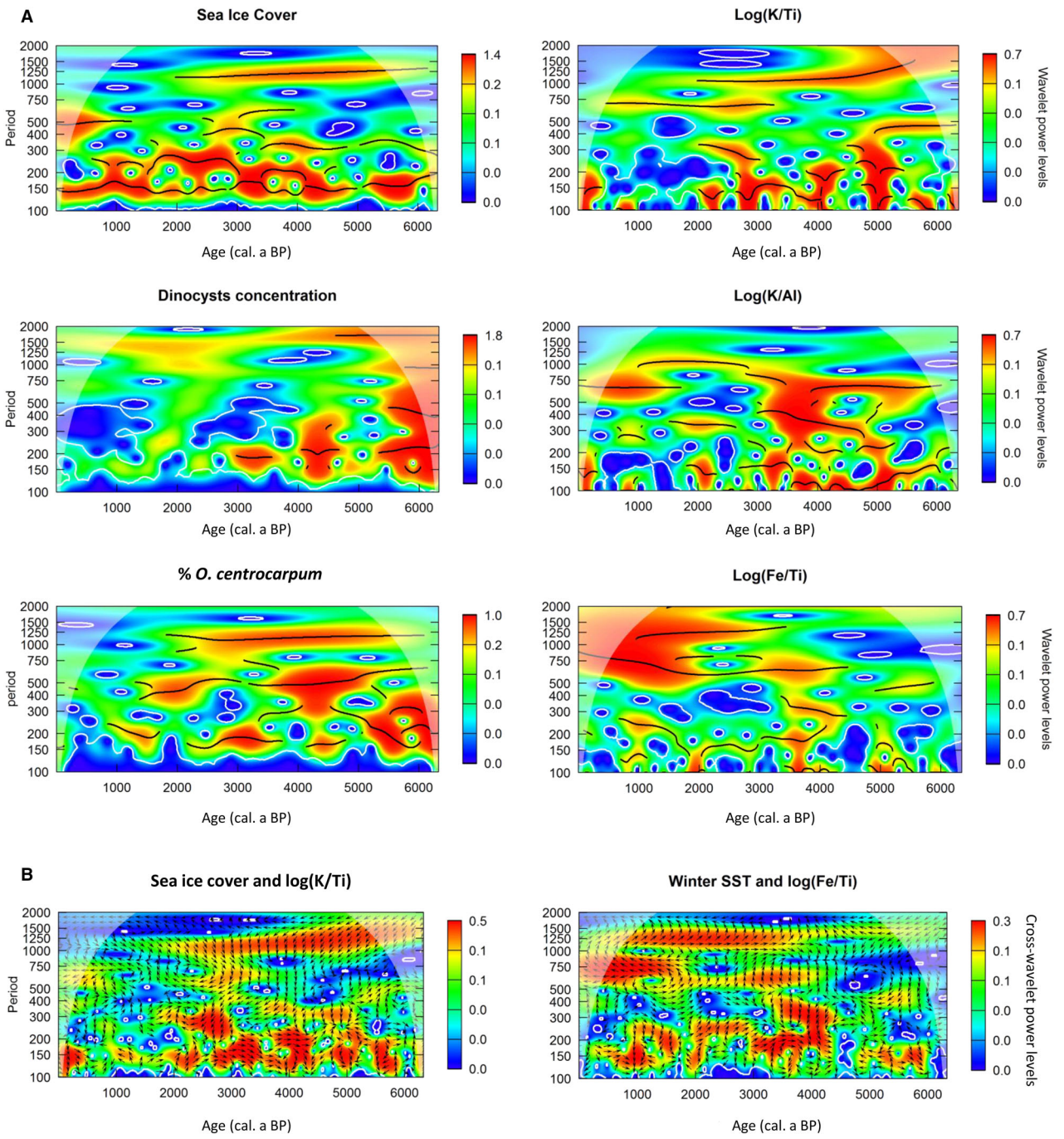

Fig. 9. Spectral analysis of the time series. A. Wavelet analysis applied on modern analogue technique reconstructions, palynological results and XRF data. B. Cross-wavelet analysis between log-ratios (K/Ti, Fe/Ti) and sea-surface conditions.

Croudace 2015), are recorded during the same period, with a marked decrease at 5.8 cal. ka BP. A change in the sediment source probably took place during that period. The sediment source could have been the eastern or inner parts of the Isfjorden fjord system, where the bedrock consists mainly of carbonate rocks and evaporites (Dallmann 2002), thus being rich in calcium and strontium. The relatively high glacial activity recorded in Billefjorden between 7.9 and 5.5 cal. ka BP, with significant ice rafting (Baeten *et al.* 2010), could explain higher sediment input from this area.

The results from the MAT also suggest an abrupt change in sea-surface conditions during this interval, with extensive sea ice cover at the base of the core, followed by a rapid decrease at 6.2 cal. ka BP. Very high percentages of the cyst of *P. dalei*, recorded between 6.7

and 6.5 cal. ka BP, may indicate stratification in surface waters related to freshwater supply from glaciers, as well as high primary productivity as reported from Svalbard fjords (Grøsfjeld *et al.* 2009). The dominance of the cyst of *P. dalei* is also roughly synchronous with the geochemical changes, suggesting that the input of meltwater with high levels of nutrients may be associated with the change in sediment source.

The onset of the major changes recorded at the base of the core was probably earlier than 6.8 cal. ka BP. It is therefore difficult to fully describe the changes without the recovery of older sediment. Nevertheless, XRF core scanning and palynology results point to a transition towards an interval marked by colder conditions. According to Forwick & Vorren (2009), the onset of a general cooling in the western Barents Sea–Svalbard region dates from 9 cal. ka BP, where it was marked by a sharp increase in iceberg and sea-ice rafting. High and fluctuating ice-rafted debris (IRD) fluxes were recorded between 9 and 4 cal. ka BP in central Isfjorden, including a peak at 7.1 cal. ka BP. This transition around 7 ka was interpreted as a regional cooling based on the foraminiferal fauna (Hald *et al.* 2004; Baeten *et al.* 2010; Skirbekk *et al.* 2010; Rasmussen *et al.* 2012) and alkenone SST estimates (van der Bilt *et al.* 2018). However, this cooling may be a feature restricted to the western Svalbard fjords, and perhaps of short duration, since glaciers reached their minimum size between 8 and 4 ka BP in the Northern Hemisphere (Solomina *et al.* 2015) and in Svalbard areas (van der Bilt *et al.* 2015; Allaart *et al.* 2020).

Zone B: Late Holocene (4.2 cal. ka BP to present)

A change in depositional regime marked the transition between zones A and B. A peak in the median grain size (Fig. 4) and a layer of coarse material led to the identification of an event at 4.4 cal. ka BP that could be associated with a small and brief ice-rafting event. Following that event, a change in sediment composition at 4.4–4.0 ka BP is recorded by the element ratios. The log(Mn/Fe) ratio, which increased sharply at ~4.2 cal. ka BP, suggests a shift towards more ventilated bottom waters. Lesser stratification in the water column associated with reduced meltwater discharge, convection with brine related to sea-ice formation or changes in bottom currents could be at the origin of enhanced bottom water ventilation. Such a shift could also be related to lower oxygen consumption from organic matter degradation. Relative concentrations of Ti and K increase significantly while relative concentrations of Al and Si record a drop during this interval (Fig. S2), highlighting a change in sediment delivery and continental weathering (Rothwell & Croudace 2015). These variations are also visible in the log-ratios K/Al and Fe/Ti. Hence, all geochemical data point towards a change in sediment delivery and bottom water conditions between 4.4 and 4.0 cal. ka BP. Changes in surface waters were recorded after, at 3.8 cal. ka BP, with a significant drop in sea ice cover during about 400 years. A marked increase in SSS seasonal contrasts and higher-amplitude variations in summer SST are also recorded from that transition. Dinocysts assemblages, dominated by *I. minutum* (~80%), record an increase in *Brigantedinium* spp., from ~15 to 40% between 4.8 and 3.8 cal. ka BP. When co-dominant, these two species reflect cold conditions and Arctic-type waters (e.g. Matthiessen *et al.* 2005; Grøsfjeld *et al.* 2009; de Vernal *et al.* 2013). Also, from about 4.2 cal. ka BP, the dinocyst *I. pallidum* shows higher abundance in the assemblage.

A transition between the Middle and Late Holocene has been observed in multiple areas worldwide. Referred to as the 4.2 ka event (see Weiss 2017), this transition was distinguished by abrupt climate changes, including megadroughts in the Middle East and Asia with collapses of societies (Weiss 2015, 2016, 2017). Bradley & Bakke (2019) reviewed palaeoclimatic studies from North Atlantic and concluded that there is no sustained evidence for the 4.2 ka event. Nevertheless, the interval spanning 4.4 to 3.8 cal. ka BP was characterized by a significant cooling step at many sites from the northeastern North Atlantic and around Svalbard (Hald *et al.* 2004; Jennings *et al.* 2004; Forwick & Vorren 2009; Skirbekk *et al.* 2010; Rasmussen *et al.* 2012; van der Bilt *et al.* 2018). In the Isfjorden fjord system, Svendsen & Mangerud (1997) concluded a major regrowth of glaciers both in the innermost part of the fjord (Billefjorden) and at the fjord mouth (Linnévatnet) from 4400 to 3600 cal. a BP. A more recent study suggested that the glaciers in the Billefjorden area started to regrow at 5470 cal. a BP (Baeten *et al.* 2010). Forwick & Vorren (2009) observed a diminution of the IRD flux at 4.0 cal. ka BP that was interpreted as being the result of enhanced formation of fast ice and/or more permanent sea ice cover leading to a reduced drift of icebergs, owing to their entrapment close to the calving fronts in tributary fjords. Although the main cause of the variations recorded in our core has not yet been demonstrated, the physical properties and geochemical data highlight an important change in the sedimentary regime. Changes in surface water proxies are not as pronounced as those of bottom-water conditions, but they occurred at around 3.8 cal. ka BP. Among the sea-surface parameters, the SSS signal captured by dinocyst assemblages is the most prominent. As mentioned above, this signal might result from generally colder conditions leading to less meltwater (higher winter salinity) but enhanced seasonal sea ice cover leading to low surface salinity in summer.

Until 2.0 cal. ka BP, the log(Mn/Fe) ratio remained high, the grain size and summer SST decreased, while the C/N ratio increased towards terrestrial values, indicating that Isfjorden was still undergoing a cooling trend. Between 2.0 and 1.2 cal. ka BP, an increase in the phototrophic taxa *Spiniferites elongatus* and *Impagi-*

dinium pallidum at the expense of *Islandinium minutum* indicates more oceanic conditions and lesser sea ice cover, thus suggesting an enhanced influence of AW (e.g. Bonnet *et al.* 2010; de Vernal *et al.* 2013). The summer SST gained ~1 °C, while sea ice cover reduced by ~1.5 months/year during this interval. With an offset of ~300 years, a change is also observed in most geochemical ratios, especially log(Mn/Fe), log(K/Al) and log(Fe/Ti), which dropped between 1.7 and 1.2 cal. ka BP. The fluctuations in geochemical content imply a decrease in bottom-water oxygenation and/or modification of sediment delivery that may be linked to an intensification of the AW advection into the Isfjorden. The preservation of foraminifera in Isfjorden also improved after 2.0 cal. ka BP with higher proportion of calcareous species, a higher concentration of agglutinated taxa and an overall increase in species diversity (Rasmussen *et al.* 2012). This indicates periodical enhanced influence of AW in bottom waters. While Rasmussen *et al.* (2012) deduced dominant AW in bottom and subsurface waters over the last 2000 years from foraminiferal assemblages, our dinocyst data rather show a transition towards colder conditions at the surface after 1.2 cal. ka BP. Sea ice cover gradually increased to 8.5 months/year, thus preventing AW from flowing at the surface. The C_{org}:N also indicates a slight shift towards more terrestrial organic inputs after 1.6 cal. ka BP.

Superimposed millennial-scale cycles

Millennial variations with two significant periods have been identified from Lomb–Scargle and wavelet analysis performed on sea-surface parameters and geochemical data. A cyclicity with a period of 1270–1300 years was identified for several proxies, but particularly for sea ice cover, the abundance of *O. centrocarpum* and the log(K/Ti) ratio. The second period was determined to be ~1590 years. Cross-wavelet analysis of geochemical composition vs. sea-surface conditions revealed a change in the phasing of the proxies between ~3.5 and ~4.5 cal. ka BP. This phase shift is synchronized with the event at 4.2–3.8 cal. ka BP described above. During the Middle Holocene, both indicators are in phase, but they change completely to anti-phase oscillation during the Late Holocene. The reason for this change in phasing still has to be elucidated but it highlights a modification of the prevailing environmental factors affecting the bottom waters vs. the surface waters.

Other studies from the North Atlantic region have reported a ~1500-year cycle during the Holocene (Bond *et al.* 1997 (Altantic, west of Iceland and west of UK); Bianchi & McCave 1999 (south Iceland basin); Oppo *et al.* 2003 (northeastern Altantic Ocean); Risebrobakken *et al.* 2003 (eastern Norwegian sea); Sarnthein *et al.* 2003 (western Barents shelf)). However, the periodicities are not constant over the entire interval, with cycles appearing to be shorter during the Early Holocene. On the western continental margin of the Barents Sea, a periodicity of 1000–1350 years was identified over the Middle and Late Holocene, while the Early Holocene was characterized by cycles of ~900 years (Sarnthein *et al.* 2003). Debret *et al.* (2007) performed wavelet analyses on the time series of Bond *et al.* (2001) and highlighted a cyclicity of 1000 years during the first half of the Holocene whereas the cycles of the last 5500 years were characterized by a period of 1500 years. The 1500-year cycles of the Holocene were initially compared to the Dansgaard/Oeschger oscillations that occurred during the last glacial period (Bond *et al.* 1997; Schulz & Paul 2002). Bond *et al.* (1997) considered the eight cooling pulses in their records as mini Dansgaard/Oeschger cycles with smaller-amplitude signals owing to smaller continental ice volumes during the Holocene than the glacial stage. The authors also interpreted the 4.2-ka event as one particularly important cooling episode. However, the linkage between these cycles, as well as their origin, remained controversial. The oscillations were tentatively attributed to solar activity (Bond *et al.* 2001), the current intensity of the North Atlantic Deep Water (Bianchi & McCave 1999; Oppo *et al.* 2003) and atmospheric processes related to the North Atlantic Oscillation (Jennings *et al.* 2002; Giraudeau *et al.* 2010). Wanner and Buetikofer (2008) reviewed 28 papers that looked into the Bond cycles phenomenon and concluded that the cycles do exist but the possible mechanisms behind them are multiple. Many studies now tend to explain this by a more complex interaction between orbital forcing, ocean circulation and volcanic eruptions (Wanner & Buetikofer 2008; Wanner *et al.* 2008, 2015; Eldevik *et al.* 2014; Solomina *et al.* 2015; Bradley & Bakke 2019; Geirsdóttir *et al.* 2019).

In our dataset from Isfjorden, the three proxies that presented the most robust millennial-scale oscillations are closely related to the AW inflow intensities. Indeed, variability in sea-ice extent and *O. centrocarpum* relative abundance reflects fluctuations of AW advection into the fjord system. Sea-ice formation depends upon surface salinity and temperature, which can vary with insolation and/or the presence of AW. In Svalbard fjords and on the shelf, *O. centrocarpum* dominates the offshore regions, where AW occupies the surface water (Grøsfjeld *et al.* 2009). The ratio log(K/Ti) can be used to compare the contribution of continental sources related to erosion, runoff and ice-rafting vs. the deposition from external sources such as material transported via the North-Atlantic current (e.g. Richter *et al.* 2006). Therefore, fluctuations in the K/Ti ratio can reflect variations in the contribution of terrestrial *vs.* North Atlantic inputs. Moreover, the MAT results show that SST and SSS maxima match sea ice cover minima, which can be an AW signal. Hence, we propose that the oscillations detected by independent tracers in the core HH16-1205-GC are related to the variations in the strength of the AW

advection in the central Isfjorden, thus there is some relationship with the dynamics of the AMOC (e.g. Kuhlbrodt *et al*. 2007). This is consistent with Debret *et al*. (2007), who concluded that during the last 5.5 ka, the strong 1500-year cycle is related to an internal oceanic variability as part of the AMOC dynamics. The solar influence is, however, not discarded as the AW is strongly influenced by incoming solar radiation and also because it probably plays a role in the global ocean circulation.

Conclusions

Cross-correlation between palynological and sedimentological data of core HH16-1205-GC provided insights into the interactions between glacier dynamics, sea-ice extent and ocean circulation. During the last ~7 ka, the central Isfjorden recorded large-amplitude changes and multiple subtle variations. One main feature is a gradual climate deterioration during the Middle and Late Holocene. At the bottom of the study core (~6.8 cal. ka BP), important variations in elements concentration (Ca, Sr, K) and percentages of the cyst *Pentapharsodinium dalei* indicate that a local cooling occurred during the transition from Early to Middle Holocene. The subsequent transition, between Middle and Late Holocene and possibly associated with the 4.2 ka event, has also been recorded in our core during the interval from 4.4 to 3.8 cal. ka BP. A marked shift in grain size and in Mn concentration, and minor variations in Fe and K, highlights a change in the depositional conditions and the ventilation of bottom water in the fjord. The SSS also indicates changes in the upper water column. A warming pulse in surface water was also recorded between 2.0 and 1.2 cal. ka BP.

The major changes recorded between 4.4 and 3.8 cal. ka BP are probably parts of the millennial-scale oscillations that characterize the hydrology of the fjord. The palynological data and the sea-surface estimates, as well as the geochemical data show a relatively strong signal of 1200–1500 year periodicity. Even though fjords are affected by local mechanisms, the millennial oscillations we have evidenced are regional as they seem to be linked to changes in the intensity of the Atlantic Water advection into the fjord. Several studies have detected similar signals in the North Atlantic region. Our data do not provide sufficient information to propose a single mechanism. However, the strong signal detected in *Operculodinium centrocarpum*, sea ice cover and log(K/Ti) together, as well as the relation between SST, SSS and sea ice cover variations, indicate that the oscillations are linked to the strength of Atlantic Water inflow into the fjord.

Acknowledgements. – This study is an ArcTrain contribution. We thank the captain and crews of RV 'Helmer Hanssen', as well as S. Iversen, who supported the core and data collection during the cruise in 2016, and T. Dahl, I. Hald and K. Monsen for their support during the laboratory work at the Department of Geosciences et UIT the Arctic University of Norway. We acknowledge the support provided by the Natural Sciences and Engineering Research Council of Canada through the Collaborative Research and Training Experience program and Discovery Grant to A. de Vernal and a scholarship grant to C. Brice. We also acknowledge complementary support from the Fonds de recherche du Québec – Nature et technologies. This research was also supported by the Basic Core Technology Development Program for the Oceans and the Polar Regions (NRF-2021M1A5A1075512, PN22013 to Seung-Il Nam) from the National Research Foundation of Korea (NRF) funded by the Ministry of Science and ICT (MSIT), Republic of Korea. Finally, we thank the people at Alfred Wegener Institut for radiocarbon analysis with the mini radiocarbon dating system. We thank S. de Schepper and one anonymous reviewer for their comments and recommendations that helped to improve this manuscript. The authors declare that they have no conflict of interest.

Author contributions. – The study was designed by CB, AdV, PF and MF. CB carried out the palynological and the sedimentological analyses and wrote the first draft of the manuscript. AdV and MF supervised the analyses. AdV and PF participated in the interpretation of data and edited the manuscript. MF and SIN were co-chiefs of the Korea–Norway joint cruise 2016 and collected the gravity core. SIN carried out the grain-size analysis.

Data availability statement. – All analytical data presented are available in the PANGAEA data repository (https://doi.pangaea.de/10.1594/PANGAEA.944722).

References

Aagaard, K., Swift, J. & Carmack, E. 1985: Thermohaline circulation in the Arctic Mediterranean seas. *Journal of Geophysical Research: Oceans 90*, 4833–4846.

Allaart, L., Müller, J., Schomacker, A., Rydningen, T. A., Håkansson, L., Kjellman, S. E., Mollenhauer, G. & Forwick, M. 2020: Late Quaternary glacier and sea-ice history of northern Wijdefjorden, Svalbard. *Boreas 49*, 417–437.

Andersen, C., Koc, N. & Moros, M. 2004: A highly unstable Holocene climate in the subpolar North Atlantic: evidence from diatoms. *Quaternary Science Reviews 23*, 2155–2166.

Baeten, N. J., Forwick, M., Vogt, C. & Vorren, T. O. 2010: Late Weichselian and Holocene sedimentary environments and glacial activity in Billefjorden, Svalbard. *Geological Society, London, Special Publications 344*, 207–223.

Berger, A. & Loutre, M.-F. 1991: Insolation values for the climate of the last 10 million years. *Quaternary Science Reviews 10*, 297–317.

Bianchi, G. G. & McCave, I. N. 1999: Holocene periodicity in North Atlantic climate and deep-ocean flow south of Iceland. *Nature 397*, 515.

van der Bilt, W. G., Bakke, J., Vasskog, K., D'Andrea, W. J., Bradley, R. S. & Ólafsdóttir, S. 2015: Reconstruction of glacier variability from lake sediments reveals dynamic Holocene climate in Svalbard. *Quaternary Science Reviews 126*, 201–218.

van der Bilt, W. G., D'Andrea, W. J., Bakke, J., Balascio, N. L., Werner, J. P., Gjerde, M. & Bradley, R. S. 2018: Alkenone-based reconstructions reveal four-phase Holocene temperature evolution for High Arctic Svalbard. *Quaternary Science Reviews 183*, 204–213.

Blaauw, M. & Christen, J. A. 2011: Flexible paleoclimate age-depth models using an autoregressive gamma process. *Bayesian Analysis 6*, 457–474.

Blott, S. J. & Pye, K. 2001: GRADISTAT: a grain size distribution and statistics package for the analysis of unconsolidated sediments. *Earth Surface Processes and Landforms 26*, 1237–1248.

Bond, G., Showers, W., Cheseby, M., Lotti, R., Almasi, P., Priore, P., Cullen, H., Hajdas, I. & Bonani, G. 1997: A pervasive millennial-scale cycle in North Atlantic Holocene and glacial climates. *Science 278*, 1257–1266.

Bond, G., Kromer, B., Beer, J., Muscheler, R., Evans, M. N., Showers, W., Hoffmann, S., Lotti-Bond, R., Hajdas, I. & Bonani, G. 2001: Persistent solar influence on North Atlantic climate during the Holocene. *Science 294*, 2130–2136.

Bonnet, S., de Vernal, A., Hillaire-Marcel, C., Radi, T. & Husum, K. 2010: Variability of sea-surface temperature and sea-ice cover in the Fram Strait over the last two millennia. *Marine Micropaleontology 74*, 59–74.

Boyer, T. P., Baranova, O. K., Coleman, C., Garcia, H. E., Grodsky, A., Locarnini, R. A., Mishonov, A. V., Paver, C. R., Reagan, J. R., Seidov, D., SmolyarI, V., Weathers, K. & Zweng, M. M. 2018: World Ocean Database 2018. *In* Mishonov, A. V. (ed.): *NOAA Atlas NESDIS 87*.

Bradley, R. & Bakke, J. 2019: Is there evidence for a 4.2 ka BP event in the northern North Atlantic region? *Climate of the Past 15*, 1665–1676.

Broecker, W. S. 2000: Was a change in thermohaline circulation responsible for the Little Ice Age? *Proceedings of the National Academy of Sciences 97*, 1339–1342.

Carlson, A. E., Stoner, J. S., Donnelly, J. P. & Hillaire-Marcel, C. 2008: Response of the southern Greenland Ice Sheet during the last two deglaciations. *Geology 36*, 359–362.

Chevalier, M., Davis, B. A., Heiri, O., Seppä, H., Chase, B. M., Gajewski, K., Lacourse, T., Telford, R. J., Finsinger, W. & Guiot, J. 2020: Pollen-based climate reconstruction techniques for late Quaternary studies. *Earth-Science Reviews 210* (103), 384, https://doi.org/10.1016/j.earscirev.2020.103384.

Cleveland, W. S. & Devlin, S. J. 1988: Locally weighted regression: an approach to regression analysis by local fitting. *Journal of the American Statistical Association 83*, 596–610.

Cottier, F., Tverberg, V., Inall, M., Svendsen, H., Nilsen, F. & Griffiths, C. 2005: Water mass modification in an Arctic fjord through cross-shelf exchange: the seasonal hydrography of Kongsfjorden, Svalbard. *Journal of Geophysical Research: Oceans 110*, C12005, https://doi.org/10.1029/2004JC002757.

Cottier, F. R., Nilsen, F., Inall, M., Gerland, S., Tverberg, V. & Svendsen, H. 2007: Wintertime warming of an Arctic shelf in response to large-scale atmospheric circulation. *Geophysical Research Letters 34*, L10607, https://doi.org/10.1029/2007GL029948.

Dallmann, W. K. 2002: *Bedrock map of Svalbard and Jan Mayen*. Temakart - Norsk polarinstitutt, ISSN 0801-8588; Nr. 33.

Debret, M., Bout-Roumazeilles, V., Grousset, F., Desmet, M., McManus, J. F., Massei, N., Sebag, D., Petit, J.-R., Copard, Y. & Trentesaux, A. 2007: The origin of the 1500-year climate cycles in Holocene North-Atlantic records. *Climate of the Past Discussions 3*, 679–692.

Dieckmann, G. S. & Hellmer, H. H. 2010: The importance of sea ice: an overview. *Sea Ice 2*, 1–22.

Diekmann, B., Hofmann, J., Henrich, R., Fütterer, D. K., Röhl, U. & Wei, K.-Y. 2008: Detrital sediment supply in the southern Okinawa Trough and its relation to sea-level and Kuroshio dynamics during the late Quaternary. *Marine Geology 255*, 83–95.

Eldevik, T., Risebrobakken, B., Bjune, A. E., Andersson, C., Birks, H. J. B., Dokken, T. M., Drange, H., Glessmer, M. S., Li, C. & Nilsen, J. E. Ø. 2014: A brief history of climate–the northern seas from the Last Glacial Maximum to global warming. *Quaternary Science Reviews 106*, 225–246.

Falardeau, J., de Vernal, A. & Spielhagen, R. F. 2018: Paleoceanography of northeastern Fram Strait since the last glacial maximum: Palynological evidence of large amplitude changes. *Quaternary Science Reviews 195*, 133–152.

Forwick, M. & Vorren, T. O. 2007: Holocene mass-transport activity and climate in outer Isfjorden, Spitsbergen: marine and subsurface evidence. *The Holocene 17*, 707–716.

Forwick, M. & Vorren, T. O. 2009: Late Weichselian and Holocene sedimentary environments and ice rafting in Isfjorden, Spitsbergen. *Palaeogeography, Palaeoclimatology, Palaeoecology 280*, 258–274.

Forwick, M., Vorren, T. O., Hald, M., Korsun, S., Roh, Y., Vogt, C. & Yoo, K.-C. 2010: Spatial and temporal influence of glaciers and rivers on the sedimentary environment in Sassenfjorden and Tempelfjorden, Spitsbergen. *Geological Society, London, Special Publications 344*, 163–193.

Geirsdóttir, Á., Miller, G. H., Andrews, J. T., Harning, D. J., Anderson, L. S., Florian, C., Larsen, D. J. & Thordarson, T. 2019: The onset of Neoglaciation in Iceland and the 4.2 ka event. *Climate of the Past 15*, 25–40.

Giraudeau, J., Grelaud, M., Solignac, S., Andrews, J., Moros, M. & Jansen, E. 2010: Millennial-scale variability in Atlantic water advection to the Nordic Seas derived from Holocene coccolith concentration records. *Quaternary Science Reviews 29*, 1276–1287.

Goslin, J., Fruergaard, M., Sander, L., Gałka, M., Menviel, L., Monkenbusch, J., Thibault, N. & Clemmensen, L. B. 2018: Holocene centennial to millennial shifts in North-Atlantic storminess and ocean dynamics. *Scientific Reports 8* (12), 778, https://doi.org/10.1038/s41598-018-29949-8.

Grøsfjeld, K., Harland, R. & Howe, J. 2009: Dinoflagellate cyst assemblages inshore and offshore Svalbard reflecting their modern hydrography and climate. *Norwegian Journal of Geology/Norsk Geologisk Forening 89*, 121–134.

Guiot, J. & de Vernal, A. 2007: Chapter thirteen transfer functions: methods for quantitative paleoceanography based on microfossils. *Developments in Marine Geology 1*, 523–563.

Guiot, J. & De Vernal, A. 2011: Is spatial autocorrelation introducing biases in the apparent accuracy of paleoclimatic reconstructions? *Quaternary Science Reviews 30*, 1965–1972.

Gurdebeke, P. R., Mertens, K. N., Takano, Y., Yamaguchi, A., Bogus, K., Dunthorn, M., Matsuoka, K., Vrielinck, H. & Louwye, S. 2018: The affiliation of Hexasterias problematica and Halodinium verrucatum sp. nov. to ciliate cysts based on molecular phylogeny and cyst wall composition. *European journal of protistology 66*, 115–135.

Hagen, J. O., Liestøl, O., Roland, E. & Jørgensen, T. 1993: *Glacier Atlas of Svalbard and Jan Mayen*. 141 pp. Norsk Polarinstitutt Meddelelser, Oslo.

Hagen, J. O., Kohler, J., Melvold, K. & Winther, J. G. 2003: Glaciers in Svalbard: mass balance, runoff and freshwater flux. *Polar Research 22*, 145–159.

Hald, M., Ebbesen, H., Forwick, M., Godtliebsen, F., Khomenko, L., Korsun, S., Ringstad Olsen, L. & Vorren, T. O. 2004: Holocene paleoceanography and glacial history of the West Spitsbergen area, Euro-Arctic margin. *Quaternary Science Reviews 23*, 2075–2088.

Heaton, T. J., Köhler, P., Butzin, M., Bard, E., Reimer, R. W., Austin, W. E., Ramsey, C. B., Grootes, P. M., Hughen, K. A. & Kromer, B. 2020: Marine20—the marine radiocarbon age calibration curve (0–55 000 cal BP). *Radiocarbon 62*, 779–820.

Heier-Nielsen, S., Conradsen, K., Heinemeier, J., Knudsen, K., Nielsen, H., Rud, N. & Sveinbjörnsdóttir, Á. 1995: Radiocarbon dating of shells and foraminifera from the Skagen core, Denmark: evidence of reworking. *Radiocarbon 37*, 119–130.

Heslop, H., De Schepper, S. & Proske, U. 2010: *Statcounts: An EXCEL Add-in to estimate required sample size and simultaneous confidence intervals for count data*.

Hohmann, S., Kucera, M. & de Vernal, A. 2020: Identifying the signature of sea-surface properties in dinocyst assemblages: Implications for quantitative palaeoceanographical reconstructions by transfer functions and analogue techniques. *Marine Micropaleontology 159*, 816, https://doi.org/10.1016/j.marmicro.2019.101816.

Howe, J. A., Harland, R., Cottier, F. R., Brand, T., Willis, K. J., Berge, J. R., Grøsfjeld, K. & Eriksson, A. 2010: Dinoflagellate cysts as proxies for palaeoceanographic conditions in Arctic fjords. *Geological Society, London, Special Publications 344*, 61–74.

Jennings, A. E., Knudsen, K. L., Hald, M., Hansen, C. V. & Andrews, J. T. 2002: A mid-Holocene shift in Arctic sea-ice variability on the East Greenland Shelf. *The Holocene 12*, 49–58.

Jennings, A. E., Weiner, N. J., Helgadottir, G. & Andrews, J. T. 2004: Modern foraminiferal faunas of the southwestern to northern Iceland shelf: oceanographic and environmental controls. *The Journal of Foraminiferal Research 34*, 180–207.

Jernas, P., Klitgaard-Kristensen, D., Husum, K., Koç, N., Tverberg, V., Loubere, P., Prins, M., Dijkstra, N. & Gluchowska, M. 2018: Annual changes in Arctic fjord environment and modern benthic foraminiferal fauna: evidence from Kongsfjorden, Svalbard. *Global and Planetary Change 163*, 119–140.

Juggins, S. 2017: *Rioja: Analysis of Quaternary Science Data, R Package Version (0.9-21)*. Available at: http://cran.r-project.org/package=rioja.

Klitgaard-Kristensen, D., Sejrup, H. & Haflidason, H. 2001: The last 18 kyr fluctuations in Norwegian Sea surface conditions and implications for the magnitude of climatic change: evidence from the North Sea. *Paleoceanography 16*, 455–467.

Knies, J. & Martinez, P. 2009: Organic matter sedimentation in the western Barents Sea region: Terrestrial and marine contribution based on isotopic composition and organic nitrogen content. *Norwegian Journal of Geology/Norsk Geologisk Forening 89*, 79–89.

Koç, N., Klitgaard-Kristensen, D., Hasle, K., Forsberg, C. F. & Solheim, A. 2002: Late glacial palaeoceanography of Hinlopen Strait, northern Svalbard. *Polar Research 21*, 307–314.

Kuhlbrodt, T., Griesel, A., Montoya, M., Levermann, A., Hofmann, M. & Rahmstorf, S. 2007: On the driving processes of the Atlantic meridional overturning circulation. *Reviews of Geophysics 45*, RG2001, https://doi.org/10.1029/2004RG000166.

Loeng, H. 1991: Features of the physical oceanographic conditions of the Barents Sea. *Polar Research 10*, 5–18.

Lomb, N. R. 1976: Least-squares frequency analysis of unequally spaced data. *Astrophysics and Space Science 39*, 447–462.

Mangerud, J. & Gulliksen, S. 1975: Apparent radiocarbon ages of recent marine shells from Norway, Spitsbergen, and Arctic Canada. *Quaternary Research 5*, 263–273.

Martín-Moreno, R., Allende Álvarez, F. & Hagen, J. O. 2017: 'Little Ice Age' glacier extent and subsequent retreat in Svalbard archipelago. *The Holocene 27*, 1379–1390.

Matthiessen, J., de Vernal, A., Head, M., Okolodkov, Y., Zonneveld, K. & Harland, R. 2005: Modem organic-walled dinoflagellate cysts in arctic marine environments and their (paleo-) environmental significance. *Paläontologische Zeitschrift 79*, 3–51.

Mayewski, P. A., Rohling, E. E., Stager, J. C., Karlén, W., Maasch, K. A., Meeker, L. D., Meyerson, E. A., Gasse, F., van Kreveld, S. & Holmgren, K. 2004: Holocene climate variability. *Quaternary Research 62*, 243–255.

McManus, J. F., Oppo, D. W. & Cullen, J. L. 1999: A 0.5-million-year record of millennial-scale climate variability in the North Atlantic. *Science 283*, 971–975.

Mertens, K. N., Verhoeven, K., Verleye, T., Louwye, S., Amorim, A., Ribeiro, S., Deaf, A. S., Harding, I. C., De Schepper, S. & González, C. 2009: Determining the absolute abundance of dinoflagellate cysts in recent marine sediments: the Lycopodium marker-grain method put to the test. *Review of Palaeobotany and Palynology 157*, 238–252.

Meyers, P. A. 1997: Organic geochemical proxies of paleoceanographic, paleolimnologic, and paleoclimatic processes. *Organic Geochemistry 27*, 213–250.

Naeher, S., Gilli, A., North, R. P., Hamann, Y. & Schubert, C. J. 2013: Tracing bottom water oxygenation with sedimentary Mn/Fe ratios in Lake Zurich, Switzerland. *Chemical Geology 352*, 125–133.

Nilsen, F., Cottier, F., Skogseth, R. & Mattsson, S. 2008: Fjord–shelf exchanges controlled by ice and brine production: the interannual variation of Atlantic Water in Isfjorden, Svalbard. *Continental Shelf Research 28*, 1838–1853.

Nuth, C., Kohler, J., König, M., Von Deschwanden, A., Hagen, J., Kääb, A., Moholdt, G. & Pettersson, R. 2013: Decadal changes from a multi-temporal glacier inventory of Svalbard. *The Cryosphere 7*, 1603–1621.

Oppo, D. W., McManus, J. F. & Cullen, J. L. 2003: Deepwater variability in the Holocene epoch. *Nature 422*, 277.

Pfeffer, W. T., Arendt, A. A., Bliss, A., Bolch, T., Cogley, J. G., Gardner, A. S., Hagen, J.-O., Hock, R., Kaser, G. & Kienholz, C. 2014: The Randolph Glacier Inventory: a globally complete inventory of glaciers. *Journal of Glaciology 60*, 537–552.

R Core Team 2021: *R: A language and environment for statistical computing*. R Foundation for Statistical Computing, Vienna, Austria.

Radi, T., Bonnet, S., Cormier, M.-A., De Vernal, A., Durantou, L., Faubert, É., Head, M. J., Henry, M., Pospelova, V. & Rochon, A. 2013: Operational taxonomy and (paleo-) autecology of round, brown, spiny dinoflagellate cysts from the Quaternary of high northern latitudes. *Marine Micropaleontology 98*, 41–57.

Rasmussen, T. L., Thomsen, E., Ślubowska, M. A., Jessen, S., Solheim, A. & Koç, N. 2007: Paleoceanographic evolution of the SW Svalbard margin (76° N) since 20,000 14C yr BP. *Quaternary Research 67*, 100–114.

Rasmussen, T. L., Forwick, M. & Mackensen, A. 2012: Reconstruction of inflow of Atlantic Water to Isfjorden, Svalbard during the Holocene: correlation to climate and seasonality. *Marine Micropaleontology 94–95*, 80–90.

Reimer, P. J., Bard, E., Bayliss, A., Beck, J. W., Blackwell, P. G., Ramsey, C. B., Buck, C. E., Cheng, H., Edwards, R. L. & Friedrich, M. 2013: IntCal13 and Marine13 radiocarbon age calibration curves 0–50,000 years cal BP. *Radiocarbon 55*, 1869–1887.

Richter, T. O., Van der Gaast, S., Koster, B., Vaars, A., Gieles, R., de Stigter, H. C., De Haas, H. & van Weering, T. C. 2006: The Avaatech XRF Core Scanner: technical description and applications to NE Atlantic sediments. *Geological Society, London, Special Publications 267*, 39–50.

Risebrobakken, B., Jansen, E., Andersson, C., Mjelde, E. & Hevrøy, K. 2003: A high-resolution study of Holocene paleoclimatic and paleoceanographic changes in the Nordic Seas. *Paleoceanography 18*, 1017, https://doi.org/10.1029/2002PA000764.

Rochon, A., de Vernal, A., Turon, J.-L., Matthießen, J. & Head, M. 1999: Distribution of recent dinoflagellate cysts in surface sediments from the North Atlantic Ocean and adjacent seas in relation to sea-surface parameters. *American Association of Stratigraphic Palynologists Contribution Series 35*, 1–146.

Roesch, A. & Schmidbauer, H. 2018: *WaveletComp: Computational Wavelet Analysis*. R package version 1.1.

Rothwell, R. & Croudace, I. 2015: Twenty years of XRF core scanning marine sediments: what do geochemical proxies tell us? *In* Croudace, I. & Rothwell, R. (eds.): *Micro-XRF Studies of Sediment Cores: Applications of a Non-Destructive Tool for the Environmental Sciences*, 25–102. Springer Netherlands, Dordrecht.

Rudels, B., Anderson, L. & Jones, E. 1996: Formation and evolution of the surface mixed layer and halocline of the Arctic Ocean. *Journal of Geophysical Research: Oceans 101*, 8807–8821.

Ruf, T. 1999: The Lomb–Scargle periodogram in biological rhythm research: analysis of incomplete and unequally spaced time-series. *Biological Rhythm Research 30*, 178–201.

Sarnthein, M., Van Kreveld, S., Erlenkeuser, H., Grootes, P., Kucera, M., Pflaumann, U. & Schulz, M. 2003: Centennial-to-millennial-scale periodicities of Holocene climate and sediment injections off the western Barents shelf, 75° N. *Boreas 32*, 447–461.

Scargle, J. D. 1982: Studies in astronomical time series analysis. II-Statistical aspects of spectral analysis of unevenly spaced data. *The Astrophysical Journal 263*, 835–853.

Schulz, M. & Paul, A. 2002: Holocene climate variability on centennial-to-millennial time scales: 1. Climate records from the North-Atlantic realm. *In* Wefer, G., Berger, W. H., Behre, K.-E. & Jansen, E. (eds.): *Climate Development and History of the North Atlantic Realm*, 41–54. Springer Berlin Heidelberg, Berlin, Heidelberg.

Serreze, M. C. & Barry, R. G. 2011: Processes and impacts of Arctic amplification: a research synthesis. *Global and Planetary Change 77*, 85–96.

Skirbekk, K., Kristensen, D. K., Rasmussen, T. L., Koç, N. & Forwick, M. 2010: Holocene climate variations at the entrance to a warm Arctic fjord: evidence from Kongsfjorden trough, Svalbard. *Geological Society, London, Special Publications 344*, 289–304.

Ślubowska, M. A., Koç, N., Rasmussen, T. L. & Klitgaard-Kristensen, D. 2005: Changes in the flow of Atlantic water into the Arctic Ocean since the last deglaciation: Evidence from the northern Svalbard continental margin, 80° N. *Paleoceanography 20*, PA4014, https://doi.org/10.1029/2005PA001141.

Solomina, O. N., Bradley, R. S., Hodgson, D. A., Ivy-Ochs, S., Jomelli, V., Mackintosh, A. N., Nesje, A., Owen, L. A., Wanner, H. & Wiles, G. C. 2015: Holocene glacier fluctuations. *Quaternary Science Reviews 111*, 9–34.

Svendsen, H., Beszczynska-Møller, A., Hagen, J. O., Lefauconnier, B., Tverberg, V., Gerland, S., Børre Ørbæk, J., Bischof, K., Papucci, C. & Zajaczkowski, M. 2002: The physical environment of Kongsfjorden–Krossfjorden, an Arctic fjord system in Svalbard. *Polar Research 21*, 133–166.

Svendsen, J. I. & Mangerud, J. 1997: Holocene glacial and climatic variations on Spitsbergen, Svalbard. *The Holocene 7*, 45–57.
Svendsen, J. I., Mangerud, J., Elverhøi, A., Solheim, A. & Schüttenhelm, R. T. 1992: The Late Weichselian glacial maximum on western Spitsbergen inferred from offshore sediment cores. *Marine Geology 104*, 1–17.
Telford, R. & Birks, H. 2009: Evaluation of transfer functions in spatially structured environments. *Quaternary Science Reviews 28*, 1309–1316.
Tjallingii, R., Röhl, U., Kölling, M. & Bickert, T. 2007: Influence of the water content on X-ray fluorescence core-scanning measurements in soft marine sediments. *Geochemistry, Geophysics, Geosystems 8*, Q02004, https://doi.org/10.1029/2006GC001393.
Van Nieuwenhove, N., Head, M. J., Limoges, A., Pospelova, V., Mertens, K. N., Matthiessen, J., De Schepper, S., de Vernal, A., Eynaud, F. & Londeix, L. 2020: An overview and brief description of common marine organic-walled dinoflagellate cyst taxa occurring in surface sediments of the Northern Hemisphere. *Marine Micropaleontology 159*, 814, https://doi.org/10.1016/j.marmicro.2019.101814.
de Vernal, A., Larouche, A. & Richard, P. H. 1987: Evaluation of palynomorph concentrations: do the aliquot and the marker-grain methods yield comparable results? *Pollen et Spores 29*, 291–303.
de Vernal, A., Henry, M. & Bilodeau, G. 2010: Micropaleontological preparation techniques and analyses. *Cahier du Geotop*. Université du Québec à Montréal, Montreal.
de Vernal, A., Hillaire-Marcel, C., Rochon, A., Fréchette, B., Henry, M., Solignac, S. & Bonnet, S. 2013: Dinocyst-based reconstructions of sea ice cover concentration during the Holocene in the Arctic Ocean, the northern North Atlantic Ocean and its adjacent seas. *Quaternary Science Reviews 79*, 111–121.
de Vernal, A., Radi, T., Zaragosi, S., Van Nieuwenhove, N., Rochon, A., Allan, E., De Schepper, S., Eynaud, F., Head, M. J. & Limoges, A. 2020: Distribution of common modern dinoflagellate cyst taxa in surface sediments of the Northern Hemisphere in relation to environmental parameters: The new n=1968 database. *Marine Micropaleontology 159*, 796, https://doi.org/10.1016/j.marmicro.2019.101796.
Wanner, H. & Buetikofer, J. 2008: Holocene Bond Cycles: real or imaginary. *Geografie 113*, 338–349.
Wanner, H., Beer, J., Bütikofer, J., Crowley, T. J., Cubasch, U., Flückiger, J., Goosse, H., Grosjean, M., Joos, F. & Kaplan, J. O. 2008: Mid-to Late Holocene climate change: an overview. *Quaternary Science Reviews 27*, 1791–1828.
Wanner, H., Mercolli, L., Grosjean, M. & Ritz, S. P. 2015: Holocene climate variability and change; a data-based review. *Journal of the Geological Society 172*, 254–263.
Wanner, H., Solomina, O., Grosjean, M., Ritz, S. P. & Jetel, M. 2011: Structure and origin of Holocene cold events. *Quaternary Science Reviews 30*, 3109–3123.
Weiss, H. 2015: Megadrought, collapse, and resilience in late 3rd millennium BC Mesopotamia. *In* Arz, H. W., Jung, R., Meller, H. & Risch, R. (eds.): *2200 BC: A Climatic Breakdown as a Cause for the Collapse of the Old World?* 35–52. Halle, Germany.
Weiss, H. 2016: Global megadrought, societal collapse and resilience at 4.2–3.9 ka BP across the Mediterranean and west Asia. *PAGES 24*, 62–63.
Weiss, H. 2017: 4.2 ka BP Megadrought and the Akkadian Collapse. *In* Weiss, H. (ed.): *Megadrought and Collapse: From Early Agriculture to Angkor*, 93–160. Oxford University Press, Oxford.
Weltje, G. J. & Tjallingii, R. 2008: Calibration of XRF core scanners for quantitative geochemical logging of sediment cores: theory and application. *Earth and Planetary Science Letters 274*, 423–438.
Werner, K., Spielhagen, R. F., Bauch, D., Hass, H. C. & Kandiano, E. 2013: Atlantic Water advection versus sea-ice advances in the eastern Fram Strait during the last 9 ka: multiproxy evidence for a two-phase Holocene. *Paleoceanography 28*, 283–295.

Supporting Information

Additional Supporting Information to this article is available at http://www.boreas.dk.

Data S1. Methodology for multivariate analyses. Multivariate analyses were performed using the R package 'vegan' (Oksanen *et al*. 2018) in order to extract common trends between dinocyst populations, sea-surface parameters and the geochemical composition of the sediment. Principal component analysis (PCA) was first applied to all data, then to a combination of environmental and chemical variables. Redundancy analysis (RDA) was necessary to compare these data with the dinocyst assemblages as the percentages of species depend upon the other variables.

Fig. S1. Median size (in micrometres) and relative percentages of sand, silt and clay of sediment samples from core HH16-1205-GC.

Fig. S2. Ratios of counts per seconds of each element over the sum of total counts. The sum includes the 11 elements used in the study, namely Al, Si, Cl, K, Ca, Ti, Mn, Fe, Rb, Sr and Zr.